The pristine dwarf-galaxy survey - IV. probing the outskirts of the dwarf galaxy Boötes I

Nicolas Longeard, Pascale Jablonka, Anke Arentsen, Guillaume F. Thomas, David S. Aguado, Raymond G. Carlberg, Romain Lucchesi, Khyati Malhan, Nicolas Martin, Alan W. Mcconnachie, et al.

Monthly Notices of the ROYAL ASTRONOMICAL SOCIETY

MNRAS **516,** 2348–2362 (2022) https://doi.org/10.1093/mnras/stac1827
Advance Access publication 2022 July 5

The Pristine dwarf galaxy survey – IV. Probing the outskirts of the dwarf galaxy Boötes I

Nicolas Longeard,[1]★ Pascale Jablonka,[1,2]★ Anke Arentsen,[3] Guillaume F. Thomas,[4,5] David S. Aguado,[6] Raymond G. Carlberg,[7] Romain Lucchesi,[1] Khyati Malhan,[8] Nicolas Martin,[3,9] Alan W. McConnachie,[10] Julio F. Navarro,[11] Rubén Sánchez-Janssen,[12] Federico Sestito,[13] Else Starkenburg[14,15] and Zhen Yuan[3]

[1]*Laboratoire d'astrophysique, École Polytechnique Fédérale de Lausanne (EPFL), Observatoire, CH-1290 Versoix, Switzerland*
[2]*GEPI, Observatoire de Paris, Université PSL, CNRS, Place Jules Janssen, F-92195 Meudon, France*
[3]*Université de Strasbourg, CNRS, Observatoire astronomique de Strasbourg, UMR 7550, F-67000 Strasbourg, France*
[4]*Instituto de Astrofísica de Canarias, Vía Láctea, E-38205 La Laguna, Tenerife, Spain*
[5]*Departamento de Astrofísica, Universidad de La Laguna, E-38206 La Laguna, Tenerife, Spain*
[6]*Institute of Astronomy, University of Cambridge, Madingley Road, Cambridge CB3 0HA, UK*
[7]*Department of Astronomy & Astrophysics, University of Toronto, Toronto, ON M5S 3H4, Canada*
[8]*The Oskar Klein Centre for Cosmoparticle Physics, Department of Physics, Stockholm University, AlbaNova, Stockholm SE-10691, Sweden*
[9]*Max-Planck-Institut für Astronomy, Königstuhl 17, D-69117 Heidelberg, Germany*
[10]*NRC Herzberg Astronomy and Astrophysics, 5071 West Saanich Road, Victoria, BC V9E 2E7, Canada*
[11]*Department of Physics and Astronomy, University of Victoria, 3800 Finnerty Road, Victoria, BC V8P 5C2, Canada*
[12]*STFC UK Astronomy Technology Centre, Royal Observatory, Blackford Hill, Edinburgh EH9 3HJ, UK*
[13]*Department of Physics and Astronomy, University of Victoria, PO Box 3055, STN CSC, Victoria, BC V8W 3P6, Canada*
[14]*Leibniz Institute for Astrophysics Potsdam (AIP), An der Sternwarte 16, D-14482 Potsdam, Germany*
[15]*Kapteyn Astronomical Institute, University of Groningen, Landleven 12, NL-9747 AD Groningen, the Netherlands*

Accepted 2022 June 17. Received 2022 June 15; in original form 2021 July 22

ABSTRACT

We present a new spectroscopic study of the dwarf galaxy Boötes I (Boo I) with data from the Anglo-Australian Telescope and its AAOmega spectrograph together with the Two Degree Field multi-object system. We observed 36 high-probability Boo I stars selected using *Gaia* Early Data Release 3 proper motions and photometric metallicities from the Pristine survey. Out of those, 27 are found to be Boo I stars, resulting in an excellent success rate of 75 per cent at finding new members. Our analysis uses a new pipeline developed to estimate radial velocities and equivalent widths of the calcium triplet lines from Gaussian and Voigt line profile fits. The metallicities of 16 members are derived, including 3 extremely metal-poor stars ([Fe/H] < -3.0), which translates into a success rate of 25 per cent at finding them with the combination of Pristine and *Gaia*. Using the large spatial extent of our new members that spans up to 4.1 half-light radii and spectroscopy from the literature, we find a systemic velocity gradient of 0.40 ± 0.10 km s^{-1} arcmin^{-1} and a small but resolved metallicity gradient of -0.008 ± 0.003 dex arcmin^{-1}. Finally, we show that Boo I is more elongated than previously thought with an ellipticity of $\epsilon = 0.68 \pm 0.15$. Its velocity and metallicity gradients as well as its elongation suggest that Boo I may have been affected by tides, a result supported by direct dynamical modelling.

Key words: galaxies: dwarf – galaxies: individual: Boötes I – Local Group.

1 INTRODUCTION

The Lambda cold dark matter cosmological model predicts the existence of low-mass, low-luminosity galaxies orbiting around massive host galaxies such as our Milky Way (MW) (Bullock, Kravtsov & Weinberg 2001; Benson, Ellis & Menanteau 2002; Wechsler 2008; Bullock & Boylan-Kolchin 2017). These satellites are also supposed to be the most dark matter (DM) dominated structures in the Universe. The first dwarf galaxies discovered almost a century ago (Sculptor and Fornax, Shapley 1938) are bright and massive objects. Together with six other discoveries that followed over the decades, they constitute the so-called classical dwarf spheroidal (dSph) satellites of the MW.

More recently, large photometric surveys such as the Sloan Digital Sky Survey (SDSS; York et al. 2000), the Panoramic Survey Telescope and Rapid Response System 3Π (PanSTARRS 3Π; Chambers et al. 2016), and the Dark Energy Survey (DES; The Dark Energy Survey Collaboration 2005) have enabled the discovery of dozens of smaller and smaller systems that are now commonly referred to as ultra-faint galaxies (UFDs). These discoveries were accompanied by efforts to spectroscopically follow up all systems that were

★ E-mail: nicolas.longeard@epfl.ch (NL); pascale.jablonka@epfl.ch (PJ)

discovered (e.g. Kleyna et al. 2005; Muñoz et al. 2006; Martin et al. 2007, 2016a; Simon & Geha 2007; Koposov et al. 2011; Kirby et al. 2013; Longeard et al. 2018, 2020). These spectroscopic observations have two main focus points, namely to derive their kinematics and their metallicity properties. In particular, the kinematics of UFD candidates are crucial as their velocity dispersion can be directly linked to their DM halo mass, should they have one (W10; Wolf et al. 2010). The DM content of all these UFDs enables direct comparison with cosmological simulations (Springel et al. 2008; Vogelsberger et al. 2014; Fattahi et al. 2016; Sawala et al. 2016; Read & Erkal 2019). However, two major assumptions are necessary to link kinematics and DM mass in the model of W10 that is widely used for UFDs: (1) the system must be in dynamical equilibrium and (2) its velocity dispersion profile must be flat, i.e. independent of the distance to the centre of the UFD.

Classical dSphs are extended with a size of several hundreds of pc (McConnachie 2012; Simon 2019) and are densely populated systems, but UFDs are much fainter and their contrast on the sky with respect to MW halo stars can be even lower. As a result, it is challenging to find members in UFDs with spectroscopy. In addition, UFDs have a typical size of tens of pc, which is larger than the field of view (FoV) of most spectrographs at their distances. As a result, the vast majority of spectroscopic campaigns targeting UFDs have been focused on their inner region (roughly within one half-light radius). These observations have been very successful at identifying a large number of member stars in these elusive systems, providing radial velocities and metallicities. They also have led to the detection of 54 extremely metal-poor (EMP) stars ([Fe/H] $<$ -3.0) in UFDs according to the Stellar Abundances for Galactic Archaeology Database (SAGA) data base (Suda et al. 2017)[1]. Such stars provide valuable information about their early formation and evolution (Tolstoy, Hill & Tosi 2009; Frebel & Norris 2015).

On the other hand, because these observations have largely targeted the inner regions of UFDs, they provide very little information on the properties of these satellites in their outer regions where departures from dynamical equilibrium and the effects of tides would be more clearly noticeable. Although such ventures into the outer regions have been attempted before (e.g. Koposov et al. 2011; Fritz et al. 2019; Chiti et al. 2021; Longeard et al. 2021), they are still limited by the observational constrains mentioned above and generally have a very low success rate in confirming members. It is therefore currently challenging to assess the reliability of the overall DM mass of UFDs known. Are all of them reliable, and if not, how many deviate from dynamical equilibrium and have more complex dynamics and/or metallicity properties?

To shed light on these two important questions, one needs to probe the outskirts of UFDs. Their stars tend to be very difficult to identify, as they are drowned by stars in the MW halo. Such studies must therefore adopt additional tools that exploit the kinematic and metallicity features that distinguish UFD stars from the MW stellar halo. Proper motions (PMs) from the *Gaia* mission (Gaia Collaboration 2018, 2021) are one of those tools, helping to identify UFD members using the systematic motion of the satellite. In addition to *Gaia*, our team benefits from the photometric metallicities of the Pristine survey (Starkenburg et al. 2010). The Pristine metallicities are reliable down to very low metallicities, and are particularly well suited to detect the metal-poor population typical of UFDs. Longeard et al. (2021) show that using Pristine alone can improve the success rate of finding new member stars by a factor of 3, from 20 per cent using only broad-band photometric constraints to 60 per cent by adding Pristine. Together, these data sets allow us to hunt for UFD member stars at large distances and to more efficiently detect EMP stars (Youakim et al. 2017; Aguado et al. 2019).

In this context, we present here a new set of spectroscopic observations of the faint UFD Boötes I (Boo I). This exceptionally large FoV combined with the *Gaia* Data Release 3 and the Pristine survey enables us to probe the outskirts of Boo I up to a distance of 4.1 half-light radii ($r_{\rm h}$). Boo I was discovered by Belokurov et al. (2006) and is the most extensively spectroscopically studied UFD (see Martin et al. 2007; Norris et al. 2008, 2010a; Koposov et al. 2011; Jenkins et al. 2021 for studies identifying new Boo I members and not reanalysing known Boo I stars at high resolution). These studies have focused on the central region of the system, with $\sim$80 per cent of the known members enclosed within $1r_{\rm h}$ and 94 per cent within $2r_{\rm h}$ to maximize the chance of finding member stars, since there should be 50 per cent of stars within $1r_{\rm h}$ and 85 per cent within $2r_{\rm h}$ when an exponential radial profile is considered. Metallicity measurements for the stars beyond $1r_{\rm h}$ only represent about 17 per cent of all Boo I members with a known [Fe/H]. Therefore, Boo I is a good target for such a study, even more so since the spectroscopy presented by Koposov et al. (2011) suggests that the kinematics of the system might be more complex that what is commonly assumed for UFDs with the possible existence of two dynamically different populations in the satellite. However, since the kinematics of Boo I can also be reasonably well described by a single population, these results are not definitive.

This work first details the new spectroscopic observations (Section 2.1), as well as the new pipeline developed by our team to derive radial velocities and metallicities from stellar spectra around the calcium triplet (CaT) region (Section 2.2). We study the kinematics and metallicity properties of Boo I in its outskirts and discuss whether its dynamics (Section 3.1) and metallicity properties (Section 3.2) exhibit spatial gradients that may reflect departure from equilibrium or the possibility that Boo I may have been affected by tidal interactions with the MW (Section 3.3). We conclude with a discussion in Section 4.

2 SPECTROSCOPIC OBSERVATIONS

This section details the selection, observations, and reduction of the data as well as our pipeline to derive radial velocities and equivalent widths from the spectra.

2.1 Data selection and acquisition

Our target selection relies on data from the Pristine survey (Starkenburg et al. 2017). Pristine is a photometric survey based on a narrow-band, metallicity-sensitive photometry centred on the calcium H&K doublet and has proven to be efficient at identifying metal-poor stars such as those characteristic of the UFDs stellar population (Youakim et al. 2017; Aguado et al. 2019; Arentsen et al. 2020; Longeard et al. 2021). Therefore, we have reliable photometric metallicity estimates for Boo I down to $g_0^{\rm SDSS} \sim 21.5$. To build our spectroscopic target list, the following criteria are used:

(i) Using the photometry from the SDSS and the Darmouth isochrone (Dotter et al. 2008) fitted to the Boo I stellar population ($A = 13$ Gyr, [Fe/H] $= -2.3$, [α/Fe] $= 0.0$, $m - M = 19.11$), we remove any star located further than 0.15 mag from the isochrone in the $[(g - i)_0, i_0]$ colour–magnitude diagram (CMD).

[1] http://sagadatabase.jp

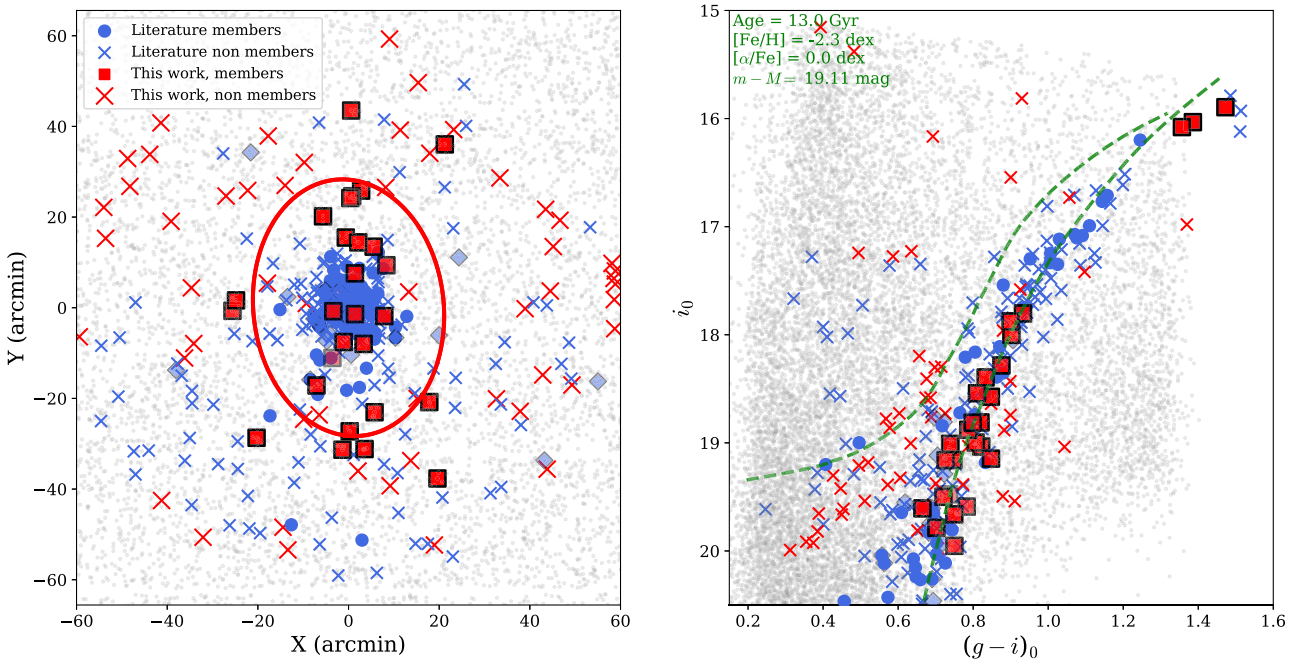

Figure 1. *Left-hand panel:* Spatial overview of the AAT spectroscopic sample. Newly discovered members are shown as red squares and their opacity depends on their dynamical membership probability. In particular, the AAT member represented with a significantly transparent symbol is the only one with a membership probability below 80 per cent, with $P_{\rm mem} \sim 60$ per cent. Non-members from the AAT sample are shown as red crosses. Previously known members from the literature are represented as smaller blue circles. Members from the literature that are not members according to this work are shown as transparent blue diamonds. The two half-light radii of Boo I as inferred by Muñoz et al. (2018, hereafter M18) are shown as a red ellipse. *Right-hand panel:* CMD of our spectroscopic sample superimposed with a metal-poor Darmouth isochrone at the distance of Boo I.

(ii) Any star with a Pristine photometric metallicity above −1.0 dex is also discarded.

(iii) When available, the PMs from the Gaia Early DR3 (eDR3; Gaia Collaboration 2021) is also used to keep only stars with a PM compatible within 2σ from that of Boo I (McConnachie & Venn 2020; Battaglia et al. 2022; $\langle \mu_\alpha^* \rangle = -0.39 \pm 0.01$ mas yr^{-1} and $\langle \mu_\delta \rangle = -1.06 \pm 0.01$ mas yr^{-1}).

These seemingly generous constraints, especially the photometric metallicity one given the systemic metallicity of the system ([Fe/H]$_{\rm BooI} \sim -2.35$ dex), are enabled by the large number of fibres available, which far exceeds our number of promising targets and allows us to cast a wide net. Finally, no stars previously observed in the literature at the time were targeted by these observations. In total, the final target list was composed of 92 stars including 36 probable Boo I red giant branch (RGB) members, 18 potential horizontal branch (HB) stars, and 12 potentially very metal-poor halo stars. The rest are low probability potential Boo I members that do not satisfy CMD or PM criteria of the 36 high probability stars but that were observed because of the large number of fibres. An overview of the spatial and CMD locations of these stars can be found in Fig. 1.

The data were obtained as a filler programme for the Pristine Inner Galaxy Survey (Arentsen et al. 2020), at the beginnings of the nights on 2020 June 16, 2020 June 17, and 2020 June 19 with two sub-exposures taken each night, on the Anglo-Australian Telescope (AAT; Saunders et al. 2004) and its AAOmega spectrograph (Lewis et al. 2002; Sharp et al. 2006) together with the Two Degree Field (2dF) multi-object system (Cannon 1997). This set-up benefits from ∼360 science fibres and ∼40 fibres for sky spectra and guiding. Only one two-degree field was needed to observe all our targets. The total exposures were divided into six sub-exposures of 2700 seconds each for a total of 4.5 h. The gratings used were 580 V for low-resolution spectra in the optical ($R \sim 1300$, 3700–5500 A), and 1700D for calcium triplet spectra with a spectral resolution R of ∼11 000. Only the red part of the spectra (from 840 to 880 nm) is used for the rest of this work.

2.2 Reduction and pipeline

The resulting spectra were reduced using the AAT 2DFDR[2] package and the standard settings, with two small exceptions. Details on the data reduction can be found in the 'Data reduction' section of Arentsen et al. (2020). Three examples of spectra for low (8.1), mid (29.0), and high (78.4) signal-to-noise (S/N) ratios are shown in Fig. 2. The S/N is computed in the CaT region.

2.2.1 Technical description of the analysis pipeline

To derive the radial velocities and equivalent widths (EWs) for the CaT lines, we developed a new pipeline that finds the continuum, performs sky-subtraction, removal of telluric lines, and fits the calcium triplet lines with both Gaussian and Voigt profiles. First, we use the method of Battaglia et al. (2008) to find the best continuum and normalize the spectra through an iterative k-sigma clipping, non-linear filter. We get rid of potential cosmic rays by discarding any emitted flux value 6σ above the continuum, with σ being the flux uncertainty of a given spectrum. The value of σ is obtained by computing the standard deviation of the continuum around the CaT lines excluding all spectral features. Sky-subtraction and removal of telluric lines are performed by minimizing the difference between

[2]https://aat.anu.edu.au/science/software/2dfdr

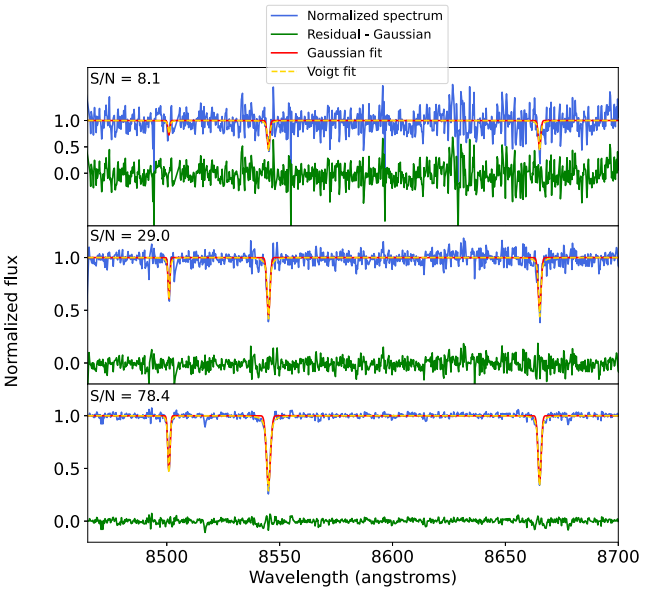

Figure 2. Spectra of three member stars in our AAT data set centred on the calcium triplet lines. Each star represents respectively the low, mid, and high S/N regimes. The normalized spectra are shown with solid blue lines while the fits derived from our pipeline for Gaussian and Voigt line profiles, detailed in Section 2.2, are shown with dashed red and yellow lines, respectively. For clarity, only the residuals in the Gaussian cases are shown (green). These stars have a radial velocity of 102.2 ± 2.8, 103.0 ± 1.0 and 102.2 ± 0.7 km s^{-1} from top to bottom.

a stellar spectrum and all the sky spectra available at the CaT lines region. Since the sky and stellar spectra can have very different fluxes, the minimization is performed by scaling the sky spectrum with a multiplying factor varying between 0.1 and 10. The best sky spectrum is then subtracted from the stellar one and this operation is repeated a second time to account for the fact that no unique sky spectrum will perfectly match the sky features present in a given stellar spectrum.

At this stage, we have normalized, cosmic rays-cleaned, sky-subtracted, and telluric-corrected spectra. Once these steps are finished, the pipeline derives the relevant scientific quantities, i.e. the radial velocity and EWs. The first step is to have a first initial guess of the radial velocity of the star. The pipeline first derives a smoothed spectrum for each star with a Gaussian kernel of width corresponding to 4 elements of resolution in order to highlight the CaT lines. We then compute the cross-correlation of these smoothed spectra with a simulated spectrum containing only the CaT lines modelled with fixed Gaussian profiles. Each Gaussian profile is defined as the following:

$$\mathcal{G}_{\rm line} = \frac{1}{\sigma_{\rm line}\sqrt{2\pi}} \exp\left(-0.5\frac{(\lambda_0 - \Delta\lambda(v))^2}{\sigma_{\rm line}^2}\right) \quad (1)$$

with $\sigma_{\rm line}$ being the standard deviation, λ_0 the theoretical location of each line at rest, and $\Delta\lambda(v)$ the Doppler shift directly linked to the radial velocity v. The Voigt profiles are defined with the approximation described by McLean, Mitchell & Swanston (1994) that takes three parameters into account: the amplitude of the Lorentzian component of the Voigt profile and the standard deviations of both the Lorentzian and Gaussian components.

In this step, only the radial velocity varies. The maximum of this correlation yields the initial radial velocity guess. The derivation of the final scientific parameters will be performed around the initial guess. Using the simulated spectrum with only the CaT lines as spectral features shifted at the initial radial velocity guess, we proceed to derive the radial velocity and EWs by fitting the spectra with a Monte Carlo Markov chain algorithm (MCMC; Hastings 1970). The central wavelengths (and therefore the radial velocities, v), the normalized fluxes of each line a_1, a_2, and a_3 as well as their standard deviations are fitted by minimizing the following likelihood:

$$\mathcal{L}_k = \frac{1}{\sigma_k\sqrt{2\pi}} \exp\left(-0.5\frac{(y_{{\rm obs},k} - y_{{\rm s},k})^2}{\sigma_k^2}\right), \quad (2)$$

where σ_k stands for the flux uncertainty for the k-th star, $y_{{\rm obs},k}$ is the observed stellar spectrum, and $y_{{\rm s},k}$ is the simulated one. The three lines are fitted simultaneously and their shapes are constrained with respect to those of the two others. The second line is constrained to be deeper than the third one which is set to be deeper than the first one. The first line also cannot be narrower than the other two. Similarly, the third line is set to be narrower than the second one.

For each star, the MCMC is ran for a million iterations and the results are chosen to be the parameters that maximize the likelihood $\mathcal{L}_k$. To obtain the EWs, each calcium triplet line from the best simulated spectrum is integrated within a 15 Å window. Finally, in the Gaussian profiles case, the EWs are divided by a factor of 1.1 to account for the poor modelling of the wings of the lines by Gaussian line profiles (Battaglia et al. 2008).

2.2.2 *Testing the pipeline's performance*

The pipeline is then thoroughly tested against previous spectroscopic studies to ensure that both the kinematics and the EWs (and therefore metallicities) are properly derived.

We take as reference 86 stars from Sextans and analysed by the *Dwarf galaxy Abundances and Radial-velocities Team* (DART; Tolstoy et al. 2006; Battaglia et al. 2011). Choosing DART is ideal as their results use the same method as our new pipeline to derive metallicities (see Section 3.2), i.e. fitting the spectra with Gaussian profiles and using the empirical calibration of Starkenburg et al. (2010) to translate the CaT EWs into [Fe/H]. Battaglia et al. (2011) also use a set-up with a resolution not too far from the one in this work ($R_{\rm DART} \sim 8000$). Since this subsample only contains stars with S/N >10, we supplement the reference sample with stars from Longeard et al. (2021) and the Sagittarius 2 globular cluster containing metal-poor stars down to a S/N of 3 to compare radial velocities in the low S/N regime. The results of this comparison are shown in Figs 3 and 4 for velocities and Fig. 5 for metallicities. They both show that our pipeline provides excellent radial velocities and metallicity measurements for all S/N regimes. By assuming that the difference between our new pipeline and DART results are normally distributed for velocities and metallicities, we find a negligible velocity bias of 0.02 ± 0.4 km s^{-1} and a scatter below 1.0 km s^{-1} at the 95 per cent confidence limit. For the metallicity, the bias, also negligible, is 0.03 ± 0.04 and the scatter below 0.09 at the 95 per cent confidence limit. Fig. 6 also shows that metallicities derived with Gaussian and Voigt line profiles are in agreement for this sample of Sextans stars with a mean difference of 0.02 ± 0.03 and a scatter below 0.08 at the 95 per cent confidence limit. These comparisons show that there is no statistically significant bias in metallicity or velocity.

3 RESULTS

We present in this section the results of our spectroscopic analysis, both dynamical and in terms of metallicity.

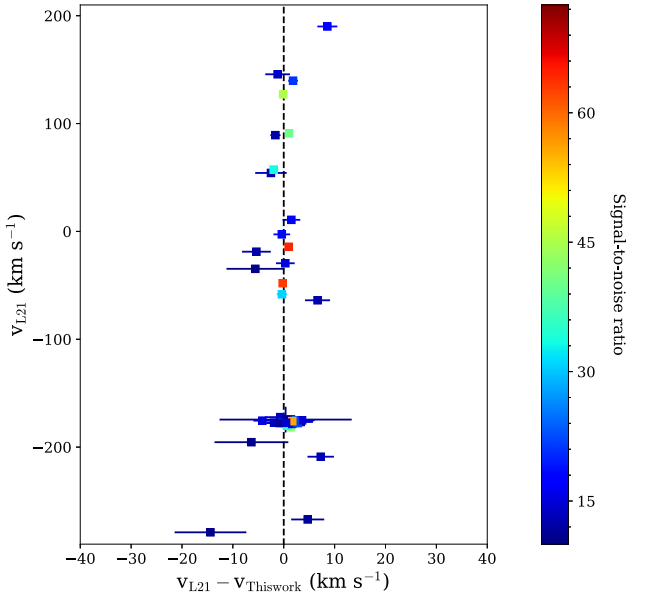

Figure 3. Difference between the radial velocities obtained with our new pipeline and the ones from L21 on the *x*-axis with respect the L21 velocities on the *y*-axis. The data are colour-coded according to their S/N ratios and the black dashed line shows the 0 km s^{-1} offset line.

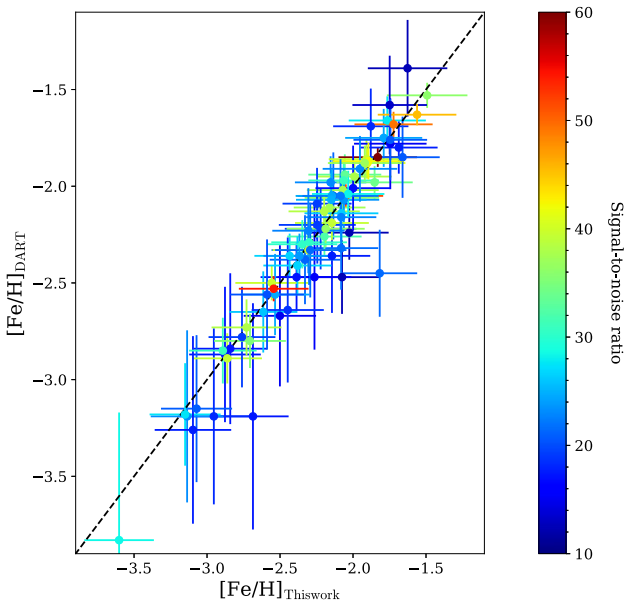

Figure 5. Comparison between the metallicities obtained with our new pipeline on the *x*-axis with the ones from the DART survey on the *y*-axis for a sample of 86 Sextans stars. The data are colour-coded according to their S/N ratios and the black dashed line shows the 1:1 line.

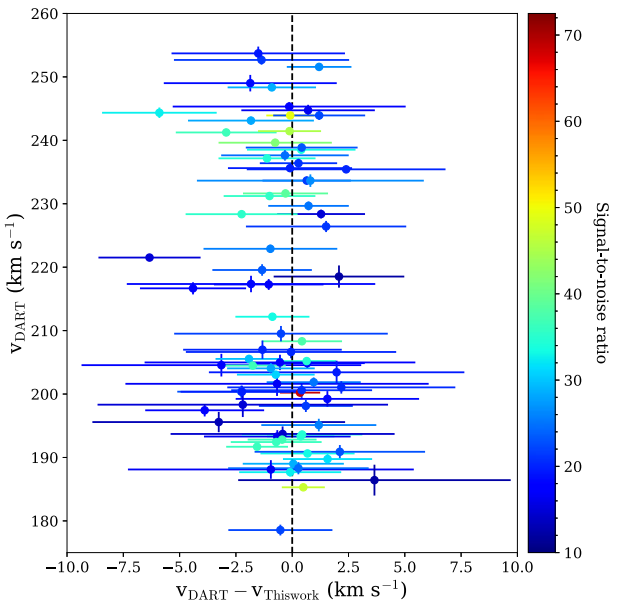

Figure 4. Difference between the radial velocities obtained with our new pipeline and the ones from DART on the *x*-axis with respect the DART velocities on the *y*-axis for a sample of 86 Sextans stars. The data are colour-coded according to their S/N ratios and the black dashed line shows the 0 km s^{-1} offset line.

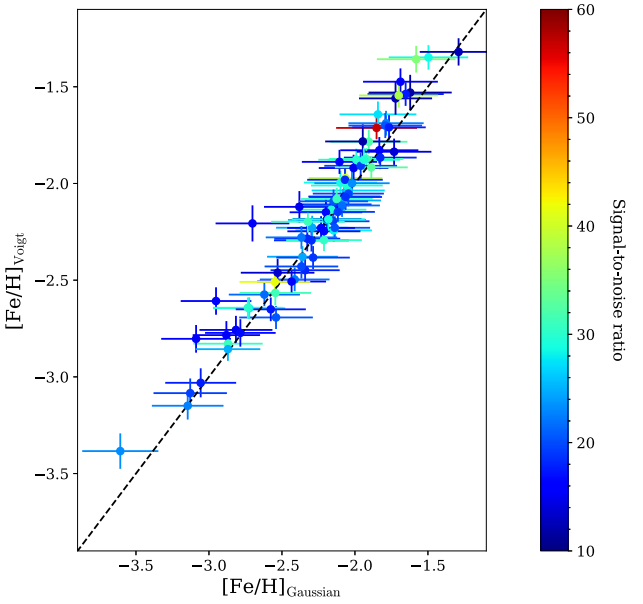

Figure 6. Comparison between the metallicities obtained with our new pipeline with Gaussian line profiles on the *x*-axis and with Voigt profiles on the *y*-axis for the sample of Sextans stars. The data are colour-coded according to their S/N ratios and the black dashed line shows the 1:1 line.

3.1 Dynamical analysis

Using the pipeline described in Section 2.2, the velocities of all stars in our sample are derived. Spectra with an S/N ratio of 3 or lower are discarded from our analysis as their resulting velocities are not reliable, leaving our spectroscopic sample with 81 stars with a median S/N of ∼9.1. To derive reliable velocity uncertainties and uncertainty floor, we apply the following relation of Li et al. (2019):

$$\delta_v = \sqrt{(1.28\delta_v^{fit})^2 + 0.66^2},$$

with δ_v^{fit} the velocity uncertainty measured by the MCMC alone, and δ_v the final uncertainty considered in the rest of this work. The main properties of the data set can be found in Table 1. The velocity distribution of the AAT sample is shown in Fig. 7 while the

Table 1. Properties of the new AAT spectroscopic sample. The individual spectroscopic metallicities for Voigt and Gaussian line profiles are reported for stars with S/N ≥10.

RA (deg)	Dec. (deg)	g_0	i_0	$CaHK_0$	v_r(km s^{-1})	μ^*_α (mas yr^{-1})	μ_δ (mas yr^{-1})	S/N	[Fe/H]$^{G}_{spectro}$	[Fe/H]$^{V}_{spectro}$	[Fe/H]$_{Pristine}$	Member
209.95887	14.3290	20.2 ± 0.0	20.2 ± 0.0	20.9 ± 0.1	107.7 ± 2.7	− 0.04 ± 0.44	− 2.13 ± 0.37	9.5	—	—	−2.27 ± 0.30	Y
209.96212	14.50078	17.4 ± 0.0	17.4 ± 0.0	18.9 ± 0.0	105.7 ± 0.7	− 0.54 ± 0.06	− 1.03 ± 0.05	64.4	−2.4 ± 0.3	−2.3 ± 0.1	−2.17 ± 0.30	Y
209.98054	14.58133	19.7 ± 0.0	19.7 ± 0.0	20.5 ± 0.1	85.0 ± 0.7	0.03 ± 0.35	− 1.35 ± 0.26	12.8	−3.5 ± 0.3	−3.5 ± 0.2	−2.14 ± 0.30	N
210.04425	14.63994	19.9 ± 0.0	19.9 ± 0.0	20.6 ± 0.1	107.5 ± 1.9	0.11 ± 0.32	− 1.19 ± 0.24	12.0	−3.1 ± 0.3	−3.0 ± 0.1	−2.42 ± 0.30	Y
210.04458	14.49011	19.6 ± 0.0	19.6 ± 0.0	20.4 ± 0.0	104.6 ± 1.4	− 0.07 ± 0.32	− 0.99 ± 0.22	12.5	−2.5 ± 0.2	−2.6 ± 0.1	−2.28 ± 0.30	Y
210.15579	14.48278	17.4 ± 0.0	17.4 ± 0.0	18.8 ± 0.0	106.5 ± 0.7	− 0.50 ± 0.06	− 1.12 ± 0.04	85.2	−2.4 ± 0.3	−2.4 ± 0.1	−1.22 ± 0.30	Y
211.031	14.43628	17.9 ± 0.0	17.9 ± 0.0	18.7 ± 0.0	− 29.2 ± 3.6	− 18.5 ± 0.10	− 24.46 ± 0.10	10.8	—	—	−0.95 ± 0.30	N
210.59508	14.99089	19.3 ± 0.0	19.3 ± 0.0	19.8 ± 0.0	40.3 ± 2.5	− 1.25 ± 0.26	− 0.38 ± 0.22	8.9	—	—	−2.64 ± 0.30	N
209.43221	14.38194	19.1 ± 0.0	19.1 ± 0.0	19.7 ± 0.0	126.8 ± 1.4	− 0.58 ± 0.22	− 1.70 ± 0.16	16.4	−2.4 ± 0.2	−2.3 ± 0.1	−2.34 ± 0.30	N
210.06792	14.94406	19.8 ± 0.0	19.8 ± 0.0	20.4 ± 0.1	104.8 ± 4.2	− 0.36 ± 0.32	− 0.93 ± 0.23	10.5	−3.3 ± 0.3	−3.1 ± 0.2	−2.56 ± 0.30	Y
210.34625	13.64131	19.7 ± 0.0	19.7 ± 0.0	20.3 ± 0.0	− 141.2 ± 5.3	− 1.22 ± 0.36	− 2.43 ± 0.31	4.8	—	—	−1.77 ± 0.30	N
210.11896	14.12933	19.8 ± 0.0	19.8 ± 0.0	20.5 ± 0.1	93.1 ± 1.4	− 0.43 ± 0.29	− 0.83 ± 0.29	11.4	−2.7 ± 0.3	−2.7 ± 0.1	−2.67 ± 0.30	Y
210.17817	13.85875	17.4 ± 0.0	17.4 ± 0.0	18.4 ± 0.0	− 64.2 ± 0.8	− 0.31 ± 0.08	− 1.77 ± 0.07	42.2	—	—	−1.78 ± 0.30	N
209.63704	14.94464	19.9 ± 0.0	19.9 ± 0.0	20.7 ± 0.1	− 110.7 ± 6.2	—	—	6.4	—	—	−1.57 ± 0.30	N
211.02067	14.67658	18.5 ± 0.0	18.5 ± 0.0	19.9 ± 0.0	− 32.5 ± 1.5	− 9.94 ± 0.14	− 8.07 ± 0.09	26.5	—	—	−0.85 ± 0.30	N
209.84958	14.10322	20.3 ± 0.0	20.3 ± 0.0	20.7 ± 0.1	123.7 ± 1.7	− 0.41 ± 0.66	− 0.85 ± 0.66	5.0	—	—	−1.57 ± 0.30	N
209.90879	14.11947	20.5 ± 0.0	20.5 ± 0.0	21.2 ± 0.1	161.3 ± 4.4	− 1.93 ± 0.58	− 2.08 ± 0.50	6.8	—	—	−1.61 ± 0.30	N
210.24858	14.57167	20.1 ± 0.0	20.1 ± 0.0	20.5 ± 0.1	− 66.7 ± 3.6	0.23 ± 0.52	− 1.07 ± 0.37	4.8	—	—	−2.39 ± 0.30	N
211.03362	14.64897	20.4 ± 0.0	20.4 ± 0.0	21.4 ± 0.1	− 60.2 ± 8.3	− 18.0 ± 0.45	− 11.75 ± 0.40	3.3	—	—	−2.05 ± 0.30	N
210.77454	13.92003	19.3 ± 0.0	19.3 ± 0.0	20.5 ± 0.0	− 34.0 ± 2.9	− 1.30 ± 0.24	− 0.89 ± 0.20	7.8	—	—	−0.97 ± 0.30	N
209.71508	15.14492	20.7 ± 0.0	20.7 ± 0.0	21.2 ± 0.1	82.6 ± 1.9	0.01 ± 0.72	− 1.35 ± 0.65	5.1	—	—	−4.04 ± 0.30	N
209.18975	14.95969	19.0 ± 0.0	19.0 ± 0.0	19.8 ± 0.0	− 43.3 ± 3.0	− 1.13 ± 0.18	− 0.26 ± 0.14	8.5	—	—	−1.52 ± 0.30	N
209.57917	14.50217	19.9 ± 0.0	19.9 ± 0.0	20.6 ± 0.1	130.4 ± 4.9	− 0.14 ± 0.37	− 1.43 ± 0.32	6.5	—	—	−2.43 ± 0.30	Y?
210.02442	14.05914	18.9 ± 0.0	18.9 ± 0.0	19.8 ± 0.0	102.9 ± 1.1	− 0.38 ± 0.19	− 0.88 ± 0.14	23.1	−2.8 ± 0.2	−2.9 ± 0.1	−2.17 ± 0.30	Y
210.32854	15.08133	19.8 ± 0.0	19.8 ± 0.0	20.9 ± 0.1	− 38.7 ± 3.7	− 1.47 ± 0.33	− 1.64 ± 0.23	10.5	—	—	−1.03 ± 0.30	N
209.42333	14.58664	20.3 ± 0.0	20.3 ± 0.0	21.0 ± 0.1	194.4 ± 4.8	− 0.28 ± 0.46	− 1.57 ± 0.36	7.8	—	—	−1.92 ± 0.30	N
209.92312	14.84953	19.2 ± 0.0	19.2 ± 0.0	19.9 ± 0.0	101.6 ± 1.7	− 0.49 ± 0.21	− 1.18 ± 0.17	14.5	−2.8 ± 0.2	−2.7 ± 0.1	−3.05 ± 0.30	Y
210.16388	14.66975	20.7 ± 0.0	20.7 ± 0.0	21.3 ± 0.1	91.4 ± 6.7	0.28 ± 0.55	− 0.77 ± 0.52	6.0	—	—	−3.98 ± 0.31	Y
210.11529	14.73794	20.5 ± 0.0	20.5 ± 0.0	21.1 ± 0.1	72.8 ± 2.0	− 0.34 ± 0.47	− 1.09 ± 0.37	5.4	—	—	−2.46 ± 0.30	N
209.46746	13.66953	18.8 ± 0.0	18.8 ± 0.0	20.1 ± 0.0	− 18.5 ± 3.2	− 0.84 ± 0.16	− 1.65 ± 0.11	8.3	—	—	−0.81 ± 0.30	N
210.08096	13.99397	18.7 ± 0.0	18.7 ± 0.0	19.6 ± 0.0	103.0 ± 1.0	− 0.27 ± 0.15	− 1.21 ± 0.12	29.0	−2.8 ± 0.2	−2.8 ± 0.1	−2.91 ± 0.30	Y
210.00167	14.38736	19.7 ± 0.0	19.7 ± 0.0	20.4 ± 0.0	101.8 ± 2.5	− 0.30 ± 0.31	− 1.16 ± 0.25	13.3	−2.9 ± 0.3	−2.9 ± 0.1	−2.52 ± 0.30	Y
209.99687	13.99147	19.7 ± 0.0	19.7 ± 0.0	20.4 ± 0.0	112.0 ± 1.4	− 0.57 ± 0.34	− 1.50 ± 0.25	8.6	—	—	−2.45 ± 0.30	Y
209.85212	15.04767	20.1 ± 0.0	20.1 ± 0.0	20.5 ± 0.1	113.2 ± 2.5	− 0.48 ± 0.44	− 1.45 ± 0.35	9.3	—	—	−2.17 ± 0.30	Y
209.34629	14.83114	20.3 ± 0.0	20.3 ± 0.0	20.8 ± 0.1	75.8 ± 1.6	0.06 ± 0.78	− 1.42 ± 0.55	3.8	—	—	−1.98 ± 0.30	N
210.17567	15.50133	18.5 ± 0.0	18.5 ± 0.0	19.4 ± 0.0	− 68.1 ± 1.3	− 0.99 ± 0.14	− 0.38 ± 0.09	17.2	—	—	−2.67 ± 0.30	N
210.030	15.23858	20.2 ± 0.0	20.2 ± 0.0	20.7 ± 0.1	93.5 ± 3.8	− 0.21 ± 0.48	− 1.03 ± 0.38	8.4	—	—	−3.99 ± 0.30	Y
209.26517	15.07736	19.7 ± 0.0	19.7 ± 0.0	20.4 ± 0.1	37.7 ± 4.6	0.72 ± 0.33	− 2.52 ± 0.27	3.9	—	—	−0.79 ± 0.30	N
210.25617	13.95158	20.2 ± 0.0	20.2 ± 0.0	20.6 ± 0.1	− 95.5 ± 5.5	0.50 ± 0.56	− 5.34 ± 0.53	7.6	—	—	−2.16 ± 0.30	N
211.02821	14.62108	16.7 ± 0.0	16.7 ± 0.0	18.0 ± 0.0	0.8 ± 1.1	− 7.00 ± 0.04	− 4.59 ± 0.04	40.1	—	—	−0.84 ± 0.30	N
210.05596	13.91322	19.5 ± 0.0	19.5 ± 0.0	20.4 ± 0.0	− 204.4 ± 3.9	− 0.45 ± 0.31	− 0.78 ± 0.24	6.8	—	—	−1.31 ± 0.30	N
211.02925	14.54336	17.7 ± 0.0	17.7 ± 0.0	18.3 ± 0.0	− 124.1 ± 3.6	− 14.91 ± 0.10	− 14.15 ± 0.09	7.2	—	—	−1.53 ± 0.30	N
209.78967	13.62336	19.6 ± 0.0	19.6 ± 0.0	20.6 ± 0.1	− 41.6 ± 2.8	− 1.25 ± 0.26	− 0.46 ± 0.21	10.4	—	—	−1.38 ± 0.30	N
210.16108	14.95578	19.6 ± 0.0	19.6 ± 0.0	20.7 ± 0.1	− 75.7 ± 1.6	− 1.30 ± 0.29	− 0.76 ± 0.20	13.9	—	—	−1.28 ± 0.30	N
210.41942	15.16842	20.2 ± 0.0	20.2 ± 0.0	20.9 ± 0.1	− 51.3 ± 6.3	− 0.93 ± 0.40	− 0.80 ± 0.31	6.0	—	—	−2.26 ± 0.30	N

Table 1 – *continued*

RA (deg)	Dec. (deg)	g_0	i_0	$CaHK_0$	v_r (km s^{-1})	μ^*_α (mas yr^{-1})	μ_δ (mas yr^{-1})	S/N	$[Fe/H]^G_{spectro}$	$[Fe/H]^V_{spectro}$	$[Fe/H]_{Pristine}$	Member
210.38567	15.11411	17.4 ± 0.0	17.4 ± 0.0	18.7 ± 0.0	102.2 ± 0.7	− 0.40 ± 0.06	− 1.02 ± 0.04	78.4	−2.5 ± 0.2	−2.5 ± 0.1	−2.46 ± 0.30	Y
210.28496	15.34111	19.9 ± 0.0	19.9 ± 0.0	20.3 ± 0.0	− 23.5 ± 33.4	− 1.60 ± 0.33	− 1.87 ± 0.26	4.8	—	—	−2.41 ± 0.30	N
210.03404	14.92353	20.4 ± 0.0	20.4 ± 0.0	21.0 ± 0.1	116.7 ± 3.5	0.43 ± 0.54	− 1.19 ± 0.41	7.3	—	—	−2.59 ± 0.30	Y
210.32679	14.16678	18.8 ± 0.0	18.8 ± 0.0	19.5 ± 0.0	102.5 ± 1.1	− 0.15 ± 0.16	− 1.03 ± 0.11	20.1	−3.0 ± 0.2	−2.8 ± 0.1	−3.10 ± 0.30	Y
210.21658	15.16669	19.3 ± 0.0	19.3 ± 0.0	19.8 ± 0.0	− 190.9 ± 5.3	− 0.61 ± 0.29	0.26 ± 0.22	10.1	—	—	−2.97 ± 0.30	N
210.69071	14.51019	19.4 ± 0.0	19.4 ± 0.0	20.1 ± 0.0	− 15.5 ± 1.9	− 0.82 ± 0.26	− 0.32 ± 0.19	9.5	—	—	−1.51 ± 0.30	N
208.9975	14.40672	15.9 ± 0.0	15.9 ± 0.0	16.6 ± 0.0	− 18.2 ± 1.1	− 18.58 ± 0.04	1.60 ± 0.03	37.4	—	—	−0.82 ± 0.30	N
209.71204	14.60381	20.0 ± 0.0	20.0 ± 0.0	20.5 ± 0.1	− 63.2 ± 1.9	− 1.90 ± 0.47	− 2.84 ± 0.38	6.1	—	—	−1.66 ± 0.30	N
210.07733	14.38042	19.4 ± 0.0	19.4 ± 0.0	20.2 ± 0.0	101.9 ± 1.5	− 0.59 ± 0.25	− 1.14 ± 0.22	17.0	−2.8 ± 0.2	−2.8 ± 0.1	−2.45 ± 0.30	Y
210.58183	14.17881	19.8 ± 0.0	19.8 ± 0.0	20.7 ± 0.1	− 92.5 ± 16.4	− 1.28 ± 0.39	− 0.73 ± 0.28	4.1	—	—	−1.61 ± 0.30	N
209.55475	14.92425	19.7 ± 0.0	19.7 ± 0.0	20.2 ± 0.0	120.6 ± 2.1	− 3.14 ± 0.35	− 2.86 ± 0.30	6.1	—	—	−1.62 ± 0.30	N
210.02658	14.91694	19.9 ± 0.0	19.9 ± 0.0	20.6 ± 0.1	98.2 ± 2.3	− 1.15 ± 0.40	− 0.94 ± 0.27	9.5	—	—	−2.30 ± 0.30	Y
210.79762	14.73847	19.0 ± 0.0	19.0 ± 0.0	19.8 ± 0.0	25.4 ± 2.1	− 1.85 ± 0.21	− 1.41 ± 0.17	16.1	—	—	−1.70 ± 0.30	N
210.00958	14.77153	19.6 ± 0.0	19.6 ± 0.0	20.2 ± 0.0	100.8 ± 1.7	− 0.13 ± 0.25	− 0.95 ± 0.20	15.6	−2.7 ± 0.3	−2.8 ± 0.1	−2.96 ± 0.30	Y
209.59275	14.54056	19.4 ± 0.0	19.4 ± 0.0	20.1 ± 0.0	114.1 ± 0.8	− 0.25 ± 0.25	− 0.80 ± 0.26	8.9	—	—	−2.30 ± 0.30	Y
209.09058	14.88239	20.3 ± 0.0	20.3 ± 0.0	20.7 ± 0.1	− 338.5 ± 1.4	− 0.54 ± 0.44	− 0.13 ± 0.36	6.2	—	—	−1.79 ± 0.30	N
209.89825	14.22769	20.0 ± 0.0	20.0 ± 0.0	21.0 ± 0.1	107.7 ± 1.9	− 0.14 ± 0.36	− 0.73 ± 0.31	10.6	−3.1 ± 0.3	−3.1 ± 0.1	−1.25 ± 0.30	Y
210.86858	14.22953	20.1 ± 0.0	20.1 ± 0.0	20.7 ± 0.1	− 127.8 ± 2.6	0.14 ± 0.41	0.29 ± 0.30	4.2	—	—	−2.41 ± 0.30	N
210.76871	14.87539	19.3 ± 0.0	19.3 ± 0.0	19.8 ± 0.0	8.5 ± 9.8	− 1.67 ± 0.24	− 3.13 ± 0.22	8.7	—	—	−2.82 ± 0.30	N
210.35771	13.88569	20.3 ± 0.0	20.3 ± 0.0	21.0 ± 0.1	102.4 ± 6.1	− 0.30 ± 0.54	− 1.25 ± 0.36	6.0	—	—	−1.90 ± 0.30	Y
209.85971	14.52906	20.4 ± 0.0	20.4 ± 0.0	20.8 ± 0.1	207.9 ± 2.6	− 0.84 ± 0.56	0.95 ± 0.43	7.3	—	—	−3.99 ± 0.30	N
210.28075	14.17983	19.6 ± 0.0	19.6 ± 0.0	20.4 ± 0.0	129.6 ± 2.7	− 0.79 ± 0.25	− 1.33 ± 0.21	6.2	—	—	−1.63 ± 0.30	N
209.39729	14.32886	19.5 ± 0.0	19.5 ± 0.0	20.1 ± 0.0	− 63.4 ± 3.9	− 0.75 ± 0.27	− 0.45 ± 0.18	11.8	—	—	−1.97 ± 0.30	N
209.09729	14.76853	19.5 ± 0.0	19.5 ± 0.0	20.4 ± 0.1	− 42.3 ± 3.0	− 1.64 ± 0.28	− 0.54 ± 0.19	4.7	—	—	−1.63 ± 0.30	N
209.18112	15.06208	20.0 ± 0.0	20.0 ± 0.0	20.5 ± 0.1	276.7 ± 5.2	− 0.91 ± 0.40	− 1.79 ± 0.32	4.0	—	—	−2.42 ± 0.30	N
209.77921	14.9630	20.0 ± 0.0	20.0 ± 0.0	20.6 ± 0.1	− 45.2 ± 2.9	− 0.74 ± 0.43	− 2.30 ± 0.34	6.9	—	—	−1.50 ± 0.30	N
210.67208	14.1325	17.8 ± 0.0	17.8 ± 0.0	19.0 ± 0.0	− 71.3 ± 0.7	− 5.99 ± 0.09	− 74.59 ± 0.06	25.1	—	—	−1.65 ± 0.30	N
209.30996	13.80478	18.9 ± 0.0	18.9 ± 0.0	19.1 ± 0.0	− 139.4 ± 0.8	0.17 ± 0.19	− 0.10 ± 0.13	9.9	—	—	−4.01 ± 0.30	N
210.78671	14.57481	15.5 ± 0.0	15.5 ± 0.0	16.2 ± 0.0	− 31.1 ± 0.8	− 0.54 ± 0.03	− 1.05 ± 0.03	90.6	—	—	−0.91 ± 0.30	N
209.3075	15.19308	19.3 ± 0.0	19.3 ± 0.0	20.1 ± 0.0	− 120.6 ± 3.3	− 0.21 ± 0.26	− 0.88 ± 0.21	8.7	—	—	−1.30 ± 0.30	N
210.82312	14.83511	20.1 ± 0.0	20.1 ± 0.0	20.5 ± 0.1	399.6 ± 4.1	0.03 ± 0.37	− 0.34 ± 0.28	4.8	—	—	—	N
210.75746	14.26647	17.9 ± 0.0	17.9 ± 0.0	18.6 ± 0.0	− 30.9 ± 2.0	0.60 ± 0.12	− 1.68 ± 0.08	17.0	—	—	−1.11 ± 0.30	N
209.77117	13.70644	18.3 ± 0.0	18.3 ± 0.0	20.0 ± 0.0	− 169.5 ± 1.7	− 86.19 ± 0.10	− 17.98 ± 0.08	18.4	—	—	−1.84 ± 0.30	N
211.03329	14.60031	16.9 ± 0.0	16.9 ± 0.0	17.8 ± 0.0	− 10.5 ± 1.3	3.98 ± 0.05	− 10.19 ± 0.04	32.7	—	—	−1.07 ± 0.30	N
209.67075	14.03533	19.2 ± 0.0	19.2 ± 0.0	19.9 ± 0.0	121.6 ± 1.0	− 0.18 ± 0.20	− 1.22 ± 0.16	13.8	−2.9 ± 0.3	−3.0 ± 0.1	−3.24 ± 0.30	Y
210.05696	14.75375	20.4 ± 0.0	20.4 ± 0.0	20.9 ± 0.1	102.2 ± 2.8	− 0.58 ± 0.48	− 1.20 ± 0.36	8.1	—	—	−3.97 ± 0.30	Y

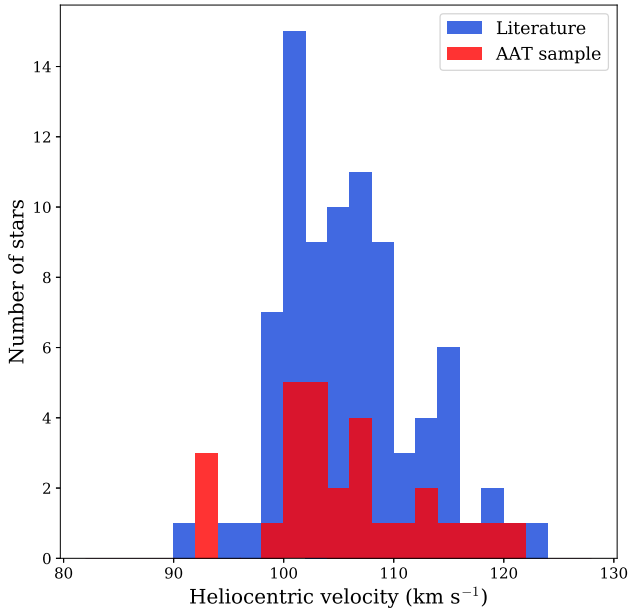

Figure 7. Radial velocity histogram of known Boo I stars from the literature (blue) and from this work (red).

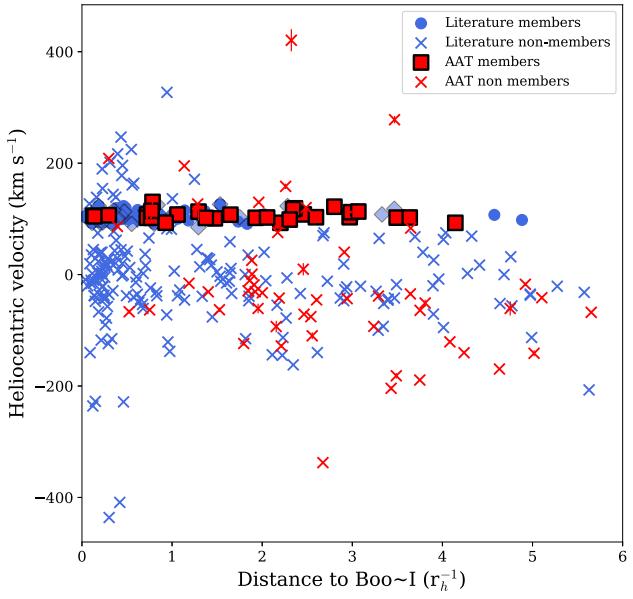

Figure 8. Radial velocities of stars from the literature (blue) and our AAT sample (red) with respect to their distance to Boo I centroid. Non-members of both the literature and the AAT sample are shown as crosses.

velocities as a function of distance are shown in Fig. 8. To assign dynamical membership probability, we derive the radial velocity and velocity dispersion of our sample, through a MCMC algorithm, by maximizing the following likelihood:

$$\mathcal{L}(\langle v_{\rm BooI}\rangle, \sigma_{\rm v}^{1}, \langle v_{\rm MW}\rangle, \sigma_{\rm v}^{\rm MW} | v_{{\rm r},k}, \delta_{{\rm v},k}) = \Pi_k (\eta_{\rm BooI} \mathcal{G}\left(v_{{\rm r},k}, \delta_{{\rm v},k} | \langle v_1\rangle, \sigma_{\rm v}^{1}\right) - (1-\eta_{\rm BooI})\mathcal{G}\left(v_{{\rm r},k}, \delta_{{\rm v},k} | \langle v_{\rm MW}\rangle, \sigma_{\rm v}^{\rm MW}\right), \quad (3)$$

with $\eta_{\rm BooI}$ the fraction of Boo I stars and $\sigma_{\rm v}^{1} = \sqrt{((\sigma_{\rm v}^{\rm BooI})^2 + \delta_{{\rm v},k}^2)}$ where $\delta_{{\rm v},k}$ is the individual velocity uncertainty of the k-th star and $\sigma_{\rm BooI}$ is the intrinsic velocity dispersion of Boo I (respectively for $\sigma_{\rm MW}$ and the MW stars). $\langle v_{\rm BooI}\rangle$ and $\langle v_{\rm MW}\rangle$ stand for the systemic radial velocity of the system and the MW stars, respectively. From this sample alone, we find a systemic radial velocity of 104.7 ± 1.6 km s^{-1} and a velocity dispersion of 9.4 ± 2.0 km s^{-1}. To identify the final number of new member stars found, both the AAT sample and the data sets from the literature are used. The literature data sets are mainly constituted of Martin et al. (2007), Norris et al. (2008, 2010a), Koposov et al. (2011), and Jenkins et al. (2021). Some of the stars in these data sets have been reobserved at higher resolution through the years (Feltzing et al. 2009; Norris et al. 2010b; Lai et al. 2011; Gilmore et al. 2013; Ishigaki et al. 2014; Frebel et al. 2016). In that case, the metallicity considered in this work (and velocity when it is also provided) is the one from higher resolution observations.

However, most of the past spectroscopic studies were conducted without the PM provided by the *Gaia* mission. Therefore, some stars identified as members by previous studies are in fact not Boo I members and are not considered so in the rest of this work. To fold in the Gaia information, the PM membership probability of each star is computed in the same fashion as Longeard et al. (2020): we fit a 2D Gaussian mixture model modelling the Boo I population and the contamination to obtain the systemic PM of the satellite and the local contamination. In order to highlight Boo I's population among field stars, this procedure is performed on a photometric sample of 1 square degree centred on the satellite for which all stars with a CMD membership probability below 1 per cent and a Pristine metallicity above −1.0 are discarded. The systemic PM obtained is similar to those of Battaglia et al. (2022) and McConnachie & Venn (2020) with $\langle \mu_\alpha^* \rangle = -0.39 \pm 0.02$ mas yr^{-1} and $\langle \mu_\delta \rangle = -1.07 \pm 0.01$ mas yr^{-1}. The resulting PM membership probabilities are folded in Eq. 3 by scaling the Gaussian distribution representing each population (Boo I and MW stars) with these probabilities. This reanalysis of the literature shows that 21 stars identified as members by previous studies have too low PM or dynamical probability membership to be considered members of the satellite. Their properties can be found in Table 2. From the entire sample, we find a systemic velocity of 103.0 ± 0.6 km s^{-1} and a velocity dispersion of 5.8 ± 0.5 km s^{-1}, consistent with the reanalysis of Boo I by Jenkins et al. (2021).

Any star with a CMD and dynamical membership probability of respectively at least 10 per cent and 50 per cent is considered a new member of Boo I. The choice for a low CMD probability threshold of 10 per cent is motivated by the fairly broad distribution of Boo I stars on its RGB (Fig. 1). We find 27 spectroscopic members. Only two of these members have a dynamical membership probability below 80 per cent (with a minimum of 60 per cent). Their velocities are shown in Fig. 7. With 36 targets being promising Boo I stars in the AAT sample, this yields a member identification success rate of 75 per cent. Among those, five were identified by Jenkins et al. (2021) shortly after our AAT data were taken and analysed.

One important aspect of this new sample is that we identified 17 stars beyond $1.0 r_{\rm h}$ of Boo I thanks to the 1 degree FoV of the AAT, therefore almost doubling the number of members known this far from the centre of the dwarf. Our furthest member is at a distance of $4.1 r_{\rm h}$. The dynamics in the outskirts of Boo I can therefore be studied. We reperform the dynamical analysis with equation (3) using subsamples from both the AAT sample and data sets from the literature. Stars are grouped by spatial bins from 0 to $3.5 r_{\rm h}$ with two different bin sizes: 0.75 and 1 arcmin. The results are presented in Fig. 9 and suggest the existence of spatial gradients. To measure it, we use the formalism of Jin & Martin (2010) and add a Gaussian

Table 2. List of previous literature members that are found not to be Boo I members in this work.

RA (deg)	Dec. (deg)	v_r (km s^{-1})	μ_α^* (mas.yr^{-1})	μ_δ (mas yr^{-1})	[Fe/H]$_{\rm spectro}$
209.9615	14.52061	85.2 ± 5.7	—	—	−2.4 ± 0.2
209.91404	14.4440	97.6 ± 7.2	0.19 ± 0.47	−1.95 ± 0.37	−2.2 ± 0.1
209.92579	14.49508	86.6 ± 1.8	−0.31 ± 0.27	−1.47 ± 0.22	−2.3 ± 0.1
210.01388	14.48097	115.9 ± 3.0	−0.97 ± 0.79	−2.19 ± 0.64	−2.5 ± 0.2
209.88962	14.47267	84.4 ± 6.6	—	—	—
209.89325	14.50478	86.0 ± 14.8	—	—	—
210.02942	14.34083	105.0 ± 10.0	−6.67 ± 0.38	−5.61 ± 0.33	—
209.94308	14.41994	91.0 ± 10.0	0.63 ± 0.48	−2.03 ± 0.38	—
209.87479	14.24908	126.0 ± 10.0	−1.30 ± 0.58	−1.04 ± 0.51	—
209.78792	14.55314	113.0 ± 10.0	−7.83 ± 0.63	−3.21 ± 0.60	—
210.96696	14.24264	123.0 ± 10.0	−6.71 ± 0.18	−8.76 ± 0.15	—
210.76388	13.95244	118.0 ± 10.0	−20.14 ± 0.28	−4.07 ± 0.22	—
210.43917	14.69853	85.0 ± 10.0	−4.10 ± 0.41	−3.29 ± 0.29	—
210.36396	14.41219	125.0 ± 10.0	−10.31 ± 0.49	2.93 ± 0.35	—
209.64854	15.08467	108.0 ± 10.0	−12.33 ± 0.69	−1.68 ± 0.54	—
209.36458	14.28411	103.0 ± 10.0	−1.17 ± 0.62	−2.26 ± 0.44	—
209.931	14.57731	100.5 ± 1.8	0.93 ± 0.77	−2.38 ± 0.66	−2.3 ± 0.2
209.93775	14.39092	102.6 ± 2.8	−0.73 ± 2.30	2.01 ± 1.76	−2.0 ± 0.3
209.9405	14.37525	90.3 ± 4.1	—	—	−2.0 ± 0.4
209.98325	14.57378	114.7 ± 0.8	−1.06 ± 0.31	−2.23 ± 0.26	−1.2 ± 0.1
210.19812	14.40333	114.0 ± 2.1	1.30 ± 0.98	−0.44 ± 0.77	−2.6 ± 0.3

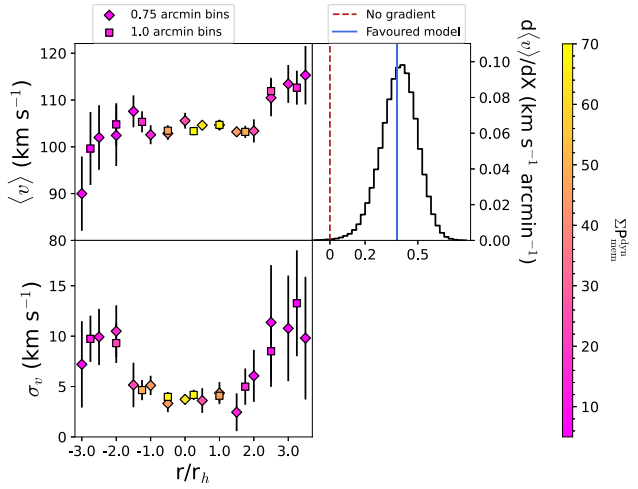

Figure 9. Systemic velocity (*top left panel*) and velocity dispersion (*bottom left panel*) as a function of the distance along the semimajor axis of Boo I, scaled by the half-light radius. Negative distances are defined as pointing towards negative declinations. Diamonds and squares respectively represent the 0.75 and 1.0 arcmin bins cases. Each point is colour-coded according to the sum of the membership probability of all stars in a given bin. The *top right panel* shows the systemic velocity gradient PDF. The red dashed line indicates the null gradient and the blue solid line the favoured model.

distribution to account for the contamination from the MW stars:

$$\mathcal{L}\left(\langle v_{\rm BooI}\rangle, \langle v_{\rm MW}\rangle, \sigma_v^{\rm BooI}, \sigma_v^{\rm MW}, {\rm d}v/{\rm d}\chi, \theta | v_{{\rm r},k}, \delta_{v,k}\right) = \Pi_k\ \eta_{\rm BooI}\left(\frac{1}{\sqrt{2\pi\sigma}}\right) \times \exp\left(\frac{1}{2}\Delta_{\rm v}/\sigma^2\right) + (1-\eta_{\rm BooI})\,\mathcal{G}\left(v_{{\rm r},k}, \delta_{{\rm v},k}, \langle v_{\rm MW}\rangle, \sigma_{\rm v}^{\rm MW}\right), \quad (4)$$

We define $\Delta_{\rm v}$ such as $\Delta_{\rm v} = {\rm v}_{{\rm r},k} - y \times {\rm d}v/{\rm d}\chi + \langle {\rm v}_{\rm BooI}\rangle$ with ${\rm d}v/{\rm d}\chi$ the systemic radial velocity gradient. y is the angular distance computed such that $y_k = X_k\cos\theta + Y_k\sin\theta$ and θ the position angle of the velocity gradient. We also define $\sigma = \sqrt{(\sigma_{\rm v}^{\rm BooI} + \delta_{\rm v}^2)}$. We emphasize that this model defines the velocity gradient as a 'linear' change from one end of the galaxy to the other. Finally, since the velocity measurements are taken from different spectroscopic data sets, such a model could be biased by systematic offsets between different spectrographs and observational set-ups. To take this into account, we follow the formalism of Minor et al. (2019) that add an offset parameter for each data set. Since they are unknown, these parameters are free and will also be derived by the MCMC algorithm.

The resulting velocity offsets between the different spectroscopic data sets are shown in Table 3 and show consistent results: data sets with the exact same set-ups (Norris et al. 2008/Norris et al. 2010a and Koposov et al. 2011/Jenkins et al. 2021) have similar offsets. Furthermore, the velocity offset between our AAT sample and Martin et al. (2007) of 7.2 ± 1.6 km s^{-1} is compatible with the one measured between our data set and the one of Norris et al. (2008) (2.8 ± 1.5 km s^{-1}) being added to the one between Norris et al. (2008) and Martin et al. (2007) as measured by the former (4.6 km s^{-1}). We detect a systemic velocity gradient of ${\rm d}v/{\rm d}\chi = 0.40 \pm 0.10$ km s^{-1} arcmin^{-1}. This translates into a ∼4.0 km s^{-1} shift per $r_{\rm h}$. To investigate whether the introduction of a gradient in the dynamical properties of the satellite impacts the velocity dispersion of Boo I and therefore its dynamical mass, they are derived without any gradient for all stars from both our sample and the previous spectroscopic studies from the literature. When no gradient is included in the dynamical model, the velocity dispersion is 5.8 ± 0.5 km s^{-1} and is larger than when it is allowed to vary with distance (4.5 ± 0.3 km s^{-1}). This result is expected since allowing the systemic velocity to vary will naturally explain part of the dispersion of individual velocities found in a system. However, it has an impact on the mass of the satellite (108 M$_\odot$ L$_\odot^{-1}$ versus 190 M$_\odot$ L$_\odot^{-1}$ without any gradient).

The bottom left panel of Fig. 9 also shows an increase of the velocity dispersion at the edges of Boo I that is a behaviour that has already been observed in UDFs (e.g. Martin et al. 2016b).

3.2 Metallicity properties

Spectroscopic metallicities are derived for the 16 member stars in our sample with an S/N ratio greater than 10 to ensure reliable

Table 3. Velocity offsets of the literature spectroscopic data sets used in this work compared to our AAT sample.

Paper	Set-up used	Velocity offset
Martin + 07	Keck/DEIMOS	7.2 ± 1.6 km s^{-1}
Norris + 08	AAT/AAOmega (blue spectra)	2.8 ± 1.5 km s^{-1}
Norris + 10	AAT/AAOmega (blue spectra)	2.6 ± 2.0 km s^{-1}
Koposov + 11	VLT/FLAMES	0.3 ± 2.8 km s^{-1}
Jenkins + 21	VLT/FLAMES	0.3 ± 1.3 km s^{-1}

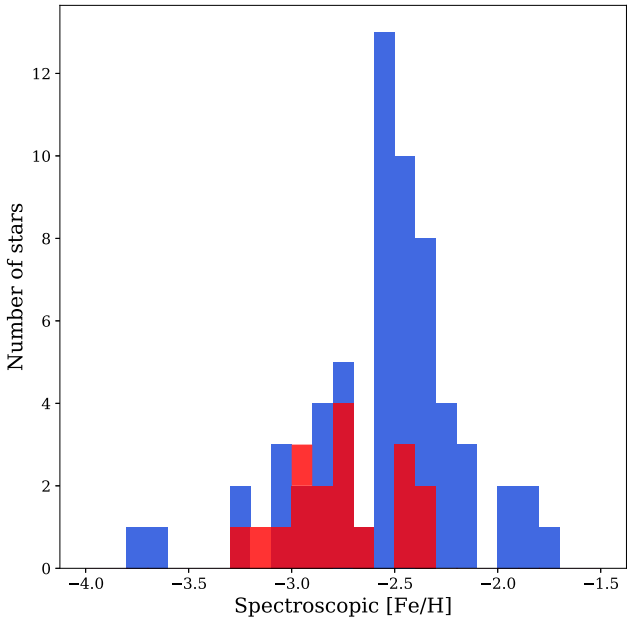

Figure 10. Spectroscopic metallicity histogram of known Boo I stars from the literature (blue) and from this work (red).

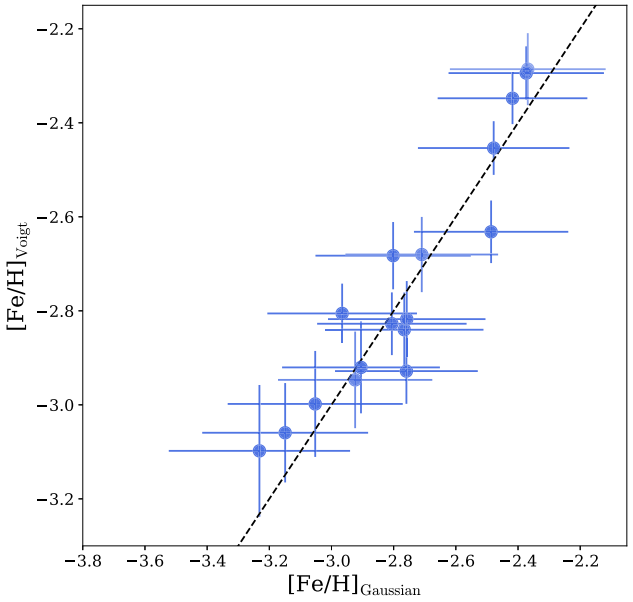

Figure 11. Comparison between the spectroscopic metallicities obtained with Gaussian line profiles and the S10 calibration on the x-axis and Voigt line profiles and the C13 calibration on the y-axis. The circles' opacity represent the dynamical membership probability of each star.

EWs measurements. Two different calibrations are used: the one of Starkenburg et al. (2010, hereafter S10) that applies for Gaussian profiles fit and the one of Carrera et al. (2013, hereafter C13) for Voigt profiles fit. Both translate the calcium triplet lines EWs into a metallicity measurement reliably down to a metallicity of −4.0.

To derive their uncertainties, we perform a Monte Carlo procedure. We randomly draw values of the EWs from their probability distribution functions (PDFs) for 10 000 iterations. At each iteration, we compute the spectroscopic metallicity. The individual photometric and Boo I distance uncertainties are also folded in in the same way. Finally, to account for the uncertainty on the calibration relation itself, we use an uncertainty of 8 per cent on each of its coefficient as specified by S10 and the proposed uncertainties on the coefficients stated by C13. For both, these uncertainties are also folded in the Monte Carlo. This process enables us to build a PDF for the metallicity of each star that takes into account the uncertainties on all the parameters involved in the derivation of the spectroscopic metallicities. The 8 per cent uncertainty of the S10 calibration naturally dominates over all other uncertainty sources, which explains the large uncertainties for the S10 calibration compared to C13.

Fig. 10 shows the resulting Voigt metallicity distribution of our sample for newly found Boo I members superimposed with the one in the literature. Fig. 11 illustrates the comparison between the metallicities obtained with Gaussian and Voigt line profiles and shows that they are perfectly compatible with a negligible bias of -0.04 ± 0.07 dex. Using the equivalent of equation (3) for the metallicities, we find a mean metallicity of -2.7 ± 0.2 and a metallicity dispersion of 0.26 ± 0.05 from the AAT sample alone. Using the whole literature yields a systemic metallicity of -2.60 ± 0.03 and a metallicity dispersion of 0.34 ± 0.03. We find a total of 3 extremely metal-poor stars (EMPs; [Fe/H] < -3.0), which accounts for almost half of the total number of EMPs known in the system according to the SAGA data base.

The metallicities as a function of distance to Boo I are shown in Fig. 12 and shows that our sample more than doubles the number of members with known spectroscopic metallicities located further than $1r_{\rm h}$ of the satellite. If the most metal-poor stars of Boo I are present at all distances, Fig. 12 hints that the more metal-rich population is more centrally concentrated as it almost disappears at a distance above $1.5r_{\rm h}$. Such a distribution is expected in higher mass dwarf galaxies in which gas tends to concentrate in the centre of the system with time, therefore giving birth to a more centrally concentrated, metal-rich population (Leaman et al. 2013; Kacharov et al. 2017; Revaz & Jablonka 2018, and references therein). To study in more details the potential spatial dependence of Boo I's metallicity properties, we perform the same analysis as in section 3.1 but for the metallicity. The results are shown in Fig. 13. We detect a small but resolved systemic metallicity gradient of -0.008 ± 0.003 dex arcmin^{-1}, translating into a ∼0.08 dex shift per $r_{\rm h}$. Our systemic metallicity is discrepant from the one of Jenkins et al. (2021), who finds a value of $-2.35^{+0.09}_{-0.08}$, at 2.9σ. Two main reasons can be

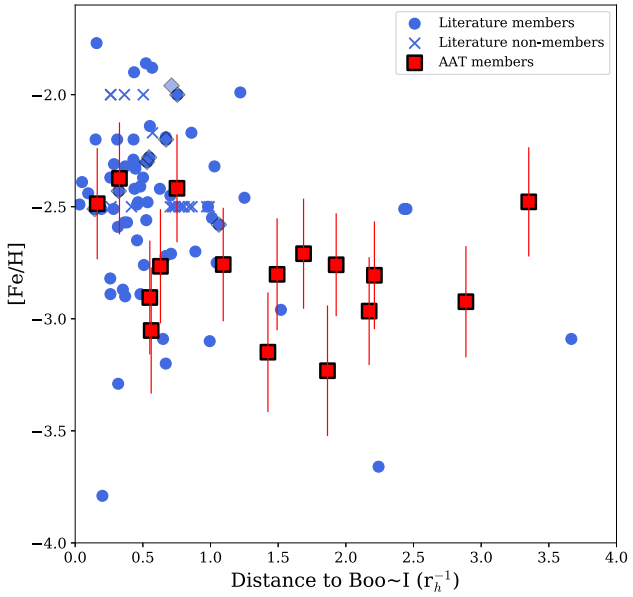

Figure 12. Spectroscopic metallicities of stars from the literature (blue) and our AAT sample (red) with respect to their distance to Boo I centroid. Blue transparent diamonds show literature members that are not compatible with the dynamical properties of Boo I found in this work. Crosses shows literature non-members.

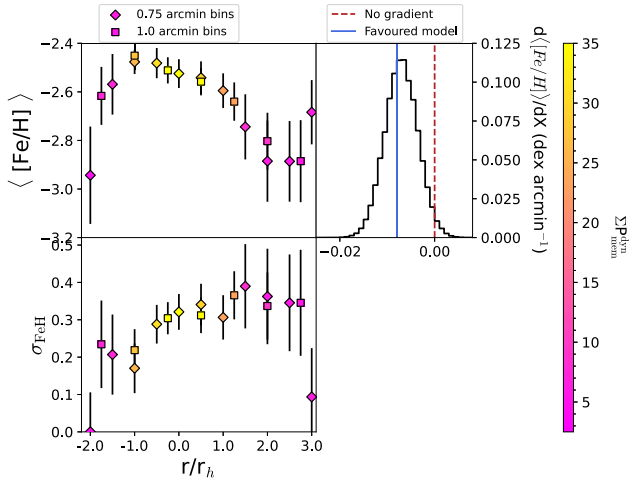

Figure 13. Similar plot as Fig. 9 for the metallicity and metallicity dispersion.

advanced to explain this discrepancy. First, this work re-analyses the entire literature with updated metallicities from subsequent higher-resolution analyses over the years, contrarily to Jenkins et al. (2021) who analyse their Very Large Telescope (VLT) sample. The second reason is that our sample is constituted of a large number of stars in the outer regions of Boo I that are more metal-poor than the rest of Boo I stars because of the existence of a negative metallicity gradient, driving the overall metallicity of our sample lower.

The bottom left panel shows no sign of a metallicity dispersion gradient. Furthermore, similarly to the case of the velocity dispersion, we find that taking a potential gradient into account deflates the metallicity dispersion to 0.26 ± 0.03 in the gradient case (versus 0.34 ± 0.03 when no gradient is being measured).

3.3 A system influenced by tides?

The detection of a systemic velocity gradient in Boo I and the spatial distribution of the new members shown in Fig. 1 begs the question of the shape of Boo I and its possible breaking of dynamical equilibrium. Even though the FoV is a two degrees diameter circle, the members appear to be distributed according to a more elongated structure aligned towards the north/south direction. Such a shape is not found by M18, who used deep photometry with a one degree square FoV and concluded that Boo I's ellipticity is low ($\epsilon_{M18} = 0.26 \pm 0.02$) assuming an exponential profile.

To investigate whether the elongated shape of Boo I detected in our data is significant, we derive the spatial profile of the system for four different cases:

(i) an SDSS purely photometric sample for which the stars are selected only based on their proximity to Boo I's RGB with any star with a $(g - i)_0$ further than 0.15 of the RGB being discarded.

(ii) a combination of the sample (i) with the *Gaia* eDR3. Using the PMs of all stars in the sample and knowing the systemic PM of Boo I (McConnachie & Venn 2020), all stars not compatible within 2σ of the system's PM are discarded.

(iii) a combination of the sample (ii) with the Pristine survey. Using the Pristine photometric metallicities, all stars with a $[Fe/H]_{Pristine} > -1.0$ are discarded.

(iv) a combination of the sample (ii) with the Pristine survey, this time limiting ourselves only to very metal-poor stars ($[Fe/H]_{Pristine} < -2.0$), much more representative the systemic metallicity of Boo I ($\langle [Fe/H]_{BooI} \rangle \sim -2.35$).

To do so, the method of Martin et al. (2007) is used. It derives spatial parameters assuming an exponential density profile for the satellite and a constant density for field stars. This exponential spatial profile can be written as

$$\rho_{dwarf}(r) = \frac{1.68^2}{2\pi r_h^2 (1-\epsilon)} \exp\left(-1.68 \frac{r}{r_h}\right). \quad (5)$$

In equation (5), ϵ is the ellipticity and r the elliptical radius defined as

$$r = \left[\left(\frac{1}{1-\epsilon} ((X - X_0)\cos\theta - (Y - Y_0)\sin\theta)^2 \right) + ((X - X_0)\sin\theta - (Y - Y_0)\cos\theta)^2 \right]^{1/2} \quad (6)$$

with X_0 and Y_0 the system's centroid and θ the position angle.

Since we use a shallower photometric sample than that of M18, the results for the sample (i) will not be exactly the same nor as precise. The goal of this analysis is to assess whether the elongated shape of the members found in this work comes from the addition, with respect to M18, of the *Gaia* PMs and/or Pristine metallicities, especially at higher distances.

The spatial distribution of the four samples is shown in Fig. 14, which shows that the elongation of Boo I is not clear with sample (i) using only photometry but becomes obvious as soon as PMs are introduced with the second sample. The shape is conserved when restricting to only very metal-poor stars according to the Pristine survey. To have a more quantitative view, the spatial properties of each sample are derived in the same way as in Martin, de Jong & Rix (2008). The resulting PDFs for the ellipticity and position angle are shown in Fig. 15. For the sample (i), i.e. photometry only, the ellipticity is not resolved. This result is compatible with the deeper data of M18. However, introducing the PMs instantly shows that Boo I is more elongated that anticipated with a position angle aligned towards the north/south direction ($\epsilon_i = 0.68 \pm 0.15$, $\theta_i = 6 \pm 24^\circ$).

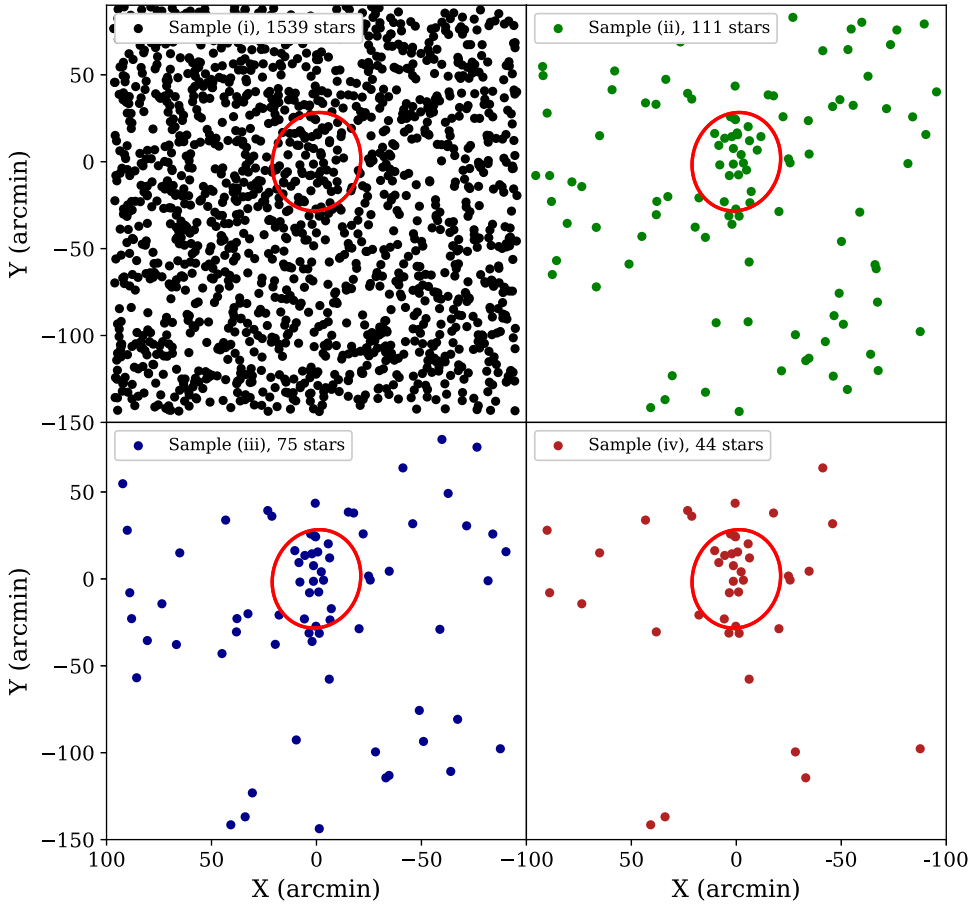

Figure 14. Spatial distributions of stars in the Boo I field for the four samples detailed in Section 3: only photometry (top left), photometry + *Gaia* (top right), photometry + *Gaia* + $[Fe/H]_{Pristine} < -1.0$ (bottom left) and photometry + *Gaia* + $[Fe/H]_{Pristine} < -2.0$ (bottom right). The two half-light radii of Boo I as derived by M18 are shown as the red ellipses.

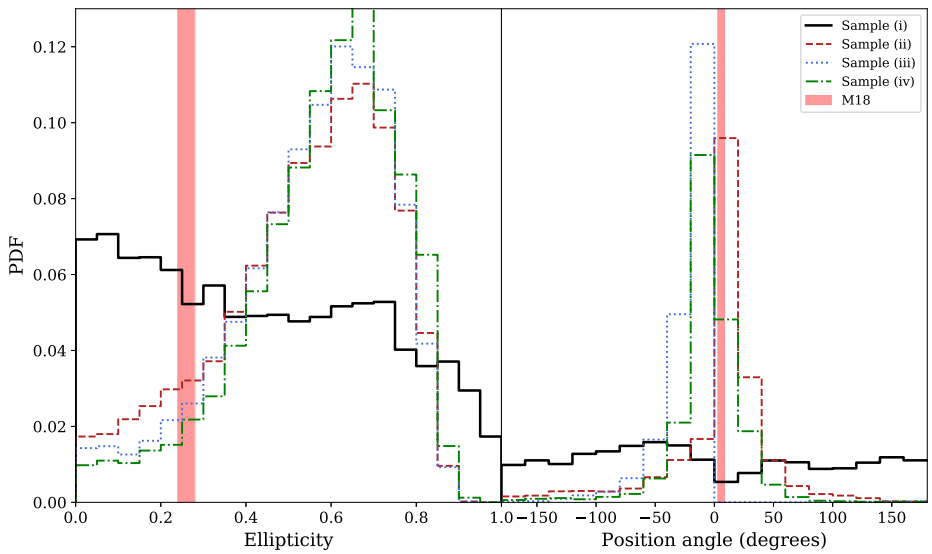

Figure 15. PDFs of the spatial parameters of Boo I for the four subsamples defined in Section 3.3 for the ellipticity (left-hand panel) and the position angle (right-hand panel). The purely photometric sample (i) is represented by the black solid lines. Adding PMs selection yields the sample (ii) shown as a red dashed line. The sample (iii) characterized by taking sample (ii) and discarding all stars with Pristine metallicities above −1.0 is shown as the blue dotted line. Finally, the fourth sample which takes sample (ii) and discards all stars with a Pristine metallicity above −2.0 is represented by the dash–dotted line. The 1σ interval of M18 are shown as the red area.

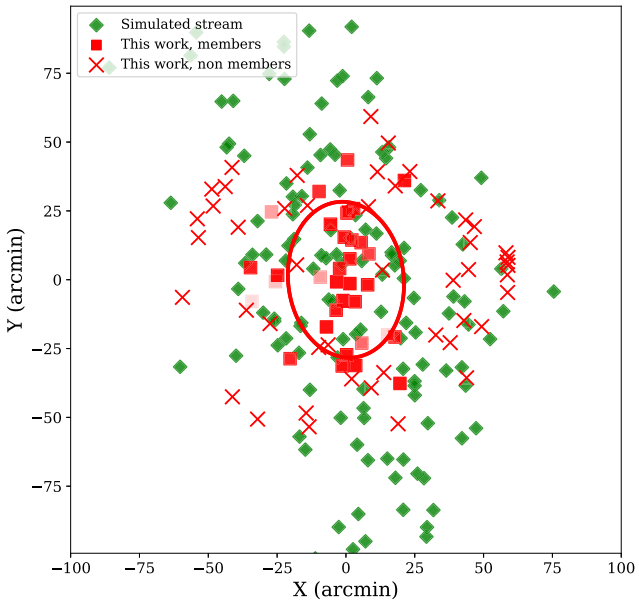

Figure 16. Spatial distribution of test particles in the hypothesis that Boo I is tidal disrupting (green diamonds) obtained with our toy model described in Section 3.3. The spectroscopic sample presented in this work is shown in red crosses (non-members) and squares (members). The two half-light radii of Boo I as derived by M18 are shown with the red ellipse.

This result is confirmed when the photometric metallicities are used to further discriminate Boo I stellar population. Furthermore, a recent study of Blue Horizontal Branch (BHB) stars in the vicinity of Boo I also finds an elongated structure in the same direction as this work (Filion & Wyse 2021).

To investigate whether this elongation could be caused by tidal interactions with the MW, we design a toy model that aims to study the spatial distribution that a tidally-disrupting Boo I should have. The model has been constructed using the particle-spraying method implemented in the GALA package (Price-Whelan et al. 2020), with a potential of the MW modelled with the MWPOTENTIAL14 of Bovy (2015) and the adopted distribution function for the stream model of Fardal, Huang & Weinberg (2015). The autogravity is taking into account where the Boo I is modelled by a Plummer sphere of mass 4.9×10^6 $M_\odot$ and with a scale radius of 0.19 kpc. In that configuration, two particles are sprayed each 0.005 Myr (1 at each Lagrange point). The resulting simulation is shown in Fig. 16 and shows that if Boo I has been tidally affected by the MW, it should be so in the North/South direction, similar to the direction found in this work using samples (ii), (iii), and (iv). The pericentre of our toy model is quite low (∼34 kpc) and similar to the pericentre in the heavy MW model of Battaglia et al. (2022) that find a pericentre of $33.70^{+8.78}_{-7.45}$ kpc. This toy model is not quantitatively perfect but shows that there is indeed an alignment between our spectroscopic members and potential tidal tails in Boo I.

Finally, our spectroscopic data do not show any trend for the PMs of members with respect to their spatial locations. However, such a trend is not necessarily expected in this case since our furthermost member is located at $4.1r_h$.

4 CONCLUSION

We observed the Boo I UFD with new mid-resolution spectroscopy using the AAT and the 2dF multi-object spectrograph to study the outskirts of the satellite. 92 stars were observed including 36 likely Boo I members based on a PM and Pristine photometric metallicity pre-selection. This pre-selection allows a significantly more successful targeting of members in the outskirts of the system with a success rate of 75 per cent at finding new Boo I stars.

We devised a new pipeline to extract the radial velocities and EWs of stellar spectra around the CaT region. This pipeline is able to fit the CaT lines with Gaussian and Voigt line profiles that allows to derive metallicities with two independent empirical calibrations, i.e. the ones of S10 and C13, respectively. It has proven to perform very well in terms of both radial velocity and metallicities at all S/N regimes when compared with the sample of L21 and 86 Sextan stars from the DART survey.

By analysing the dynamical properties of this new sample, 27 spectroscopically confirmed Boo I stars are found. Thanks to the wide FoV of 2dF, 17 members were identified at a distance larger than $1r_h$ of Boo I with the furthermost member at $4.1r_h$, doubling the number of stars known above $1r_h$. Among those, 12 are located further than $2r_h$ (versus 5 in the literature). The spatial extent of the spectroscopic sample allows us to detect a systemic velocity gradient of 0.40 ± 0.10 km s^{-1} arcmin^{-1}. Furthermore, the metallicities of 16 of the new members are derived using our new pipeline and the calibrations of S10 and C13. We detect a metallicity gradient in Boo I of -0.008 ± 0.003 dex arcmin^{-1}. Such a detection is not surprising in dwarf galaxies but has mostly been measured in brighter classical dSph and irregular galaxies, such as Phoenix (Kacharov et al. 2017) or WLM (Leaman et al. 2013). These metallicity gradients also appear in simulations (Benítez-Llambay et al. 2016; Revaz & Jablonka 2018; Mercado et al. 2021). Such a phenomenon is caused by the fact that the gas from which the stars were formed is more centrally concentrated over time, leading to metal-rich stars being preferentially found in the inner region of the galaxy, while older, more metal-poor stars will be distributed more homogeneously across the system. This has been shown in several classical dwarfs such as Sculptor (de Boer et al. 2012a) and Fornax (de Boer et al. 2012b). However, it is only the second time that a significant metallicity gradient is measured in a UFD after Tucana II (Chiti et al. 2021). Furthermore, the high-resolution spectroscopic analysis of Mashonkina et al. (2017) shows that its knee in α element abundance, if confirmed, implies that Boo I was able to reprocess supernova Ia ejecta, which would bring the satellite closer to massive UFDs and classical dwarf galaxies rather than to very low-mass UFDs.

Finally, despite our circular field of view and no a priori shape criterion to identify targets, the spatial distribution of member stars is noticeably elongated. This is in contrast with M18, who report a fairly spherical shape of Boo I ($\epsilon_{M18} = 0.26 \pm 0.02$). We have investigated this by studying the shape of the satellite in four cases: (i) using only photometry; (ii) adding PMs; (iii) discarding all stars of (ii) with a Pristine photometric metallicity above -1.0; and (iv) discarding all stars of (ii) with a Pristine photometric metallicity above -2.0. When using only photometry, the analysis yields a shape compatible with previous findings with $\epsilon_i < 0.3$ at the 1σ level; adding PMs to discriminate between Boo I and field stars yields a very elongated shape with $\epsilon_i = 0.68 \pm 0.13$ following the position angle $\theta_i = 6 \pm 24$ towards the north/east direction. This result is confirmed when restricting the sample by using photometric metallicities. We investigate whether tidal interactions are a plausible origin to explain this shape and the spatial dependence of the satellite's dynamical properties. To do so, a toy model of a tidally disrupting Boo I under a realistic MW potential is performed and shows that, should Boo I

be sufficiently affected by tides, the latter would be oriented in the same direction as that found for Boo I in samples (ii), (iii), and (iv).

Combining the elongation of the satellite, the detection of both a systemic velocity and metallicity gradient, the α element abundance from previous studies, and the low pericentre of the satellite as derived by Battaglia et al. (2022) suggests that Boo I could have been more massive than it is today and that the satellite is currently significantly affected by tidal interactions with the MW.

ACKNOWLEDGEMENTS

This work has been carried out thanks to the support of the Swiss National Science Foundation.

AA and NFM acknowledge funding from the European Research Council (ERC) under the European Union's Horizon 2020 research and innovation programme (grant agreement no. 834148).

ES acknowledges funding through VIDI grant 'Pushing Galactic Archaeology to its limits' (with project number VI.Vidi.193.093), which is funded by the Dutch Research Council (NWO).

NFM and ZY gratefully acknowledge support from the French National Research Agency (ANR) funded project Pristine (ANR-18-CE31-0017) along with funding from CNRS/INSU through the Programme National Galaxies et Cosmologie and through the CNRS grant PICS07708.

This study is based on observations obtained with MegaPrime/MegaCam, a joint project of CFHT and CEA/DAPNIA, at the Canada–France–Hawaii Telescope (CFHT), which is operated by the National Research Council (NRC) of Canada, the Institut National des Science de l'Univers of the Centre National de la Recherche Scientifique (CNRS) of France, and the University of Hawaii.

The authors thank the International Space Science Institute, Bern, Switzerland for providing financial support and meeting facilities to the international team Pristine.

This work has made use of data from the European Space Agency (ESA) mission *Gaia* (https://www.cosmos.esa.int/gaia), processed by the Gaia Data Processing and Analysis Consortium (DPAC, https://www.cosmos.esa.int/web/gaia/dpac/consortium). Funding for the DPAC has been provided by national institutions, in particular the institutions participating in the Gaia Multilateral Agreement.

The Pan-STARRS1 Surveys (PS1) and the PS1 public science archive have been made possible through contributions by the Institute for Astronomy, the University of Hawaii, the Pan-STARRS Project Office, the Max-Planck Society and its participating institutes, the Max Planck Institute for Astronomy, Heidelberg and the Max Planck Institute for Extraterrestrial Physics, Garching, The Johns Hopkins University, Durham University, the University of Edinburgh, the Queen's University Belfast, the Harvard–Smithsonian Center for Astrophysics, the Las Cumbres Observatory Global Telescope Network Incorporated, the National Central University of Taiwan, the Space Telescope Science Institute, the National Aeronautics and Space Administration under grant no. NNX08AR22G issued through the Planetary Science Division of the NASA Science Mission Directorate, the National Science Foundation grant no. AST-1238877, the University of Maryland, Eotvos Lorand University (ELTE), the Los Alamos National Laboratory, and the Gordon and Betty Moore Foundation.

This work is based (in part) on data obtained at Siding Spring Observatory (via programme A/2020A/11). We acknowledge the traditional custodians of the land on which the AAT stands, the Gamilaraay people, and pay our respects to elders past and present.

We thank Sven Buder, Sarah Martell, and Daniel Zucker who observed the AAT data used in this work.

DATA AVAILABILITY

The data underlying this article are available in the article.

REFERENCE

Aguado D. S. et al., 2019, MNRAS, 490, 2241
Arentsen A. et al., 2020, MNRAS, 496, 4964
Battaglia G., Irwin M., Tolstoy E., Helmi A., Letarte B., Jablonka P., 2008, MNRAS, 383, 183
Battaglia G., Taibi S., Thomas G. F., Fritz T. K., 2022, A&A, 657, A54
Battaglia G., Tolstoy E., Helmi A., Irwin M., Parisi P., Hill V., Jablonka P., 2011, MNRAS, 411, 1013
Belokurov V. et al., 2006, ApJ, 647, L111
Benítez-Llambay A., Navarro J. F., Abadi M. G., Gottlöber S., Yepes G., Hoffman Y., Steinmetz M., 2016, MNRAS, 456, 1185
Benson A. J., Ellis R. S., Menanteau F., 2002, MNRAS, 336, 564
Bovy J., 2015, ApJS, 216, 29
Bullock J. S., Boylan-Kolchin M., 2017, ARA&A, 55, 343
Bullock J. S., Kravtsov A. V., Weinberg D. H., 2001, ApJ, 548, 33
Cannon R. D., 1997, in Kontizas E., Kontizas M., Morgan D. H., Vettolani G. P., eds, 2dF: the Two-Degree Field Facility on the AAT, Vol. 212. Springer, Dordrecht, p. 33
Carrera R., Pancino E., Gallart C., del Pino A., 2013, MNRAS, 434, 1681 (C13)
Chambers K. C. et al., 2016, preprint (arXiv:1612.05560)
Chiti A. et al., 2021, Nat. Astron., 5, 392
de Boer T. J. L. et al., 2012a, A&A, 539, A103
de Boer T. J. L. et al., 2012b, A&A, 544, A73
Dotter A., Chaboyer B., Jevremović D., Kostov V., Baron E., Ferguson J. W., 2008, ApJS, 178, 89
Fardal M. A., Huang S., Weinberg M. D., 2015, MNRAS, 452, 301
Fattahi A. et al., 2016, MNRAS, 457, 844
Feltzing S., Eriksson K., Kleyna J., Wilkinson M. I., 2009, A&A, 508, L1
Filion C., Wyse R. F. G., 2021, ApJ, 923, 218
Frebel A., Norris J. E., 2015, ARA&A, 53, 631
Frebel A., Norris J. E., Gilmore G., Wyse R. F. G., 2016, ApJ, 826, 110
Fritz T. K., Carrera R., Battaglia G., Taibi S., 2019, A&A, 623, A129
Gaia Collaboration, 2018, A&A, 616, A1
Gaia Collaboration, 2021, A&A, 649, A1
Gilmore G., Norris J. E., Monaco L., Yong D., Wyse R. F. G., Geisler D., 2013, ApJ, 763, 61
Hastings W. K., 1970, Biometrika, 57, 97
Ishigaki M. N., Aoki W., Arimoto N., Okamoto S., 2014, A&A, 562, A146
Jenkins S. A., Li T. S., Pace A. B., Ji A. P., Koposov S. E., Mutlu-Pakdil B., 2021, ApJ, 920, 92
Jin S., Martin N. F., 2010, ApJ, 721, 1333
Kacharov N. et al., 2017, MNRAS, 466, 2006
Kirby E. N., Boylan-Kolchin M., Cohen J. G., Geha M., Bullock J. S., Kaplinghat M., 2013, ApJ, 770, 16
Kleyna J. T., Wilkinson M. I., Evans N. W., Gilmore G., 2005, ApJ, 630, L141
Koposov S. E. et al., 2011, ApJ, 736, 146
Lai D. K., Lee Y. S., Bolte M., Lucatello S., Beers T. C., Johnson J. A., Sivarani T., Rockosi C. M., 2011, ApJ, 738, 51
Leaman R. et al., 2013, ApJ, 767, 131
Lewis I. J. et al., 2002, MNRAS, 333, 279
Li T. S. et al., 2019, MNRAS, 490, 3508
Longeard N. et al., 2018, MNRAS, 480, 2609
Longeard N. et al., 2020, MNRAS, 491, 356
Longeard N. et al., 2021, MNRAS, 503, 2754
Martin N. F. et al., 2016a, MNRAS, 458, L59
Martin N. F. et al., 2016b, ApJ, 818, 40
Martin N. F., de Jong J. T. A., Rix H.-W., 2008, ApJ, 684, 1075

Martin N. F., Ibata R. A., Chapman S. C., Irwin M., Lewis G. F., 2007, MNRAS, 380, 281
Mashonkina L., Jablonka P., Sitnova T., Pakhomov Y., North P., 2017, A&A, 608, A89
McConnachie A. W., 2012, AJ, 144, 4
McConnachie A. W., Venn K. A., 2020, AJ, 160, 124
McLean A., Mitchell C., Swanston D., 1994, J. Electron Spectrosc. Relat. Phenom., 69, 125
Mercado F. J. et al., 2021, MNRAS, 501, 5121
Minor Q. E., Pace A. B., Marshall J. L., Strigari L. E., 2019, MNRAS, 487, 2961
Muñoz R. R., Carlin J. L., Frinchaboy P. M., Nidever D. L., Majewski S. R., Patterson R. J., 2006, ApJ, 650, L51
Muñoz R. R., Côté P., Santana F. A., Geha M., Simon J. D., Oyarzún G. A., Stetson P. B., Djorgovski S. G., 2018, ApJ, 860, 66 (M18)
Norris J. E., Gilmore G., Wyse R. F. G., Wilkinson M. I., Belokurov V., Evans N. W., Zucker D. B., 2008, ApJ, 689, L113
Norris J. E., Wyse R. F. G., Gilmore G., Yong D., Frebel A., Wilkinson M. I., Belokurov V., Zucker D. B., 2010a, ApJ, 723, 1632
Norris J. E., Yong D., Gilmore G., Wyse R. F. G., 2010b, ApJ, 711, 350
Price-Whelan A. et al., 2020, adrn/gala: v1.3
Read J. I., Erkal D., 2019, MNRAS, 487, 5799
Revaz Y., Jablonka P., 2018, A&A, 616, A96
Saunders W. et al., 2004, in Moorwood A. F. M., Iye M., eds, Proc. SPIE Conf. Ser. Vol. 5492, Ground-Based Instrumentation for Astronomy. SPIE, Bellingham, p. 389
Sawala T. et al., 2016, MNRAS, 457, 1931
Shapley H., 1938, Nature, 142, 715
Sharp R. et al., 2006, in McLean I. S., Iye M., eds, Proc. SPIE Conf. Ser. Vol. 6269, Ground-Based and Airborne Instrumentation for Astronomy. SPIE, Bellingham, p. 62690G
Simon J. D., 2019, ARA&A, 57, 375
Simon J. D., Geha M., 2007, ApJ, 670, 313
Springel V. et al., 2008, MNRAS, 391, 1685
Starkenburg E. et al., 2010, A&A, 513, A34 (S10)
Starkenburg E. et al., 2017, MNRAS, 471, 2587
Suda T. et al., 2017, PASJ, 69, 76
The Dark Energy Survey Collaboration, 2005, preprint (arXiv:astro-ph/0510346)
Tolstoy E. et al., 2006, The Messenger, 123, 33
Tolstoy E., Hill V., Tosi M., 2009, ARA&A, 47, 371
Vogelsberger M. et al., 2014, MNRAS, 444, 1518
Wechsler R. H., 2008, in Kodama T., Yamada T., Aoki K., eds, ASP Conf. Ser. Vol. 399, Panoramic Views of Galaxy Formation and Evolution. Astron. Soc. Pac., San Francisco, p. 82
Wolf J., Martinez G. D., Bullock J. S., Kaplinghat M., Geha M., Muñoz R. R., Simon J. D., Avedo F. F., 2010, MNRAS, 406, 1220
York D. G. et al., 2000, AJ, 120, 1579
Youakim K. et al., 2017, MNRAS, 472, 2963

This paper has been typeset from a TEX/LATEX file prepared by the author.